

# Treatment of uncertainties in multi-physics model for wind turbine asset management



Elias FEKHARI

ÉLECTRICITÉ DE FRANCE R&D

*Chatou, France*

&

CÔTE D'AZUR UNIVERSITY

*Nice, France*

This dissertation is submitted for the degree of

*Doctor of Philosophy*

Pr. Mireille BOSSY,	INRIA, Sophia-Antipolis	Examiner
Dr. Vincent CHABRIDON	EDF R&D, Chatou	Co-advisor
Dr. Sébastien DA VEIGA	ENSAI, Rennes	Examiner
Dr. Bertrand IOOSS	EDF R&D, Chatou	Thesis director
Dr. Joseph MURÉ	EDF R&D, Chatou	Co-advisor
Pr. Franck SCHOEFS	Nantes Université, Nantes	Reviewer
Pr. Daniel STRAUB	TUM, Munich	Reviewer
Pr. Bruno SUDRET	ETH, Zürich	Examiner



# Table of contents

List of figures	vii
List of tables	ix
Introduction	1
<b>I Introduction to treatment of uncertainties and wind energy</b>	<b>3</b>
<b>1 Treatment of uncertainties in computer experiments</b>	<b>5</b>
1.1 Introduction . . . . .	5
1.2 Problem specification (step A) . . . . .	5
1.2.1 Black-box computer model . . . . .	5
1.2.2 Output quantity of interest . . . . .	5
1.3 Input uncertainty quantification (step B) . . . . .	5
1.3.1 Joint probability distribution [copulogram package] . . . . .	5
1.3.2 Parametric multivariate estimation . . . . .	5
1.3.3 Non-parametric multivariate estimation . . . . .	5
1.3.4 Goodness-of-fit . . . . .	5
1.4 Uncertainty propagation for central tendency estimation (step C) . . . . .	5
1.4.1 Numerical integration . . . . .	5
1.4.2 Numerical design of experiments . . . . .	6
1.4.3 Central tendency estimation . . . . .	7
1.5 Uncertainty propagation for rare event estimation (step C) . . . . .	7
1.5.1 Problem formalization . . . . .	7
1.5.2 Rare event estimation methods . . . . .	7
1.6 Sensitivity analysis (step C') . . . . .	7
1.6.1 Global sensitivity analysis . . . . .	7
1.6.2 Reliability-oriented sensitivity analysis . . . . .	7
1.7 Metamodeling . . . . .	7
1.7.1 Global metamodel . . . . .	7
1.7.2 Reliability-oriented metamodel . . . . .	7

1.8	Conclusion . . . . .	7
<b>2</b>	<b>Introduction to wind turbine modeling and design</b>	<b>9</b>
2.1	Introduction . . . . .	10
2.2	Wind turbine modeling . . . . .	10
2.2.1	Synthetic wind generation [ <b>TurbSim, Kaimal spectrum</b> ] . . . . .	10
2.2.2	Synthetic wave generation . . . . .	10
2.2.3	Aerodynamic interactions . . . . .	10
2.2.4	Servo-Hydro-Aero-Elastic wind turbine simulation [ <b>DIEGO</b> ] . . . . .	10
2.2.5	Soil modeling . . . . .	10
2.2.6	Wake modeling [ <b>FarmShadow</b> ] . . . . .	10
2.3	Recommended design practices . . . . .	10
2.3.1	Design load cases . . . . .	10
2.3.2	Dynamic response design . . . . .	10
2.3.3	Fatigue response design . . . . .	10
2.4	Uncertain inputs . . . . .	10
2.4.1	Environmental inputs . . . . .	10
2.4.2	System inputs . . . . .	10
2.4.3	Probabilistic fatigue assessment . . . . .	10
2.5	Conclusion . . . . .	10
<b>II</b>	<b>Contributions to uncertainty quantification and propagation</b>	<b>11</b>
<b>3</b>	<b>Kernel-based uncertainty quantification</b>	<b>13</b>
3.1	Introduction . . . . .	13
3.2	Nonparametric fit of the environmental inputs . . . . .	13
3.3	Quantifying and clustering the wake-induced perturbations within a wind farm . . . . .	13
3.3.1	Uncertainty propagation in a wake model . . . . .	15
3.3.2	Statistical metric of wake-induced perturbations . . . . .	17
3.3.3	Conclusion . . . . .	18
3.4	Conclusion . . . . .	20
<b>4</b>	<b>Kernel-based central tendency estimation</b>	<b>21</b>
4.1	Introduction . . . . .	21
4.2	Treatment of uncertainties on the Teesside wind farm . . . . .	23
4.2.1	Numerical simulation model . . . . .	23
4.2.2	Measured environmental data . . . . .	24
4.2.3	Non parametric fit with empirical Bernstein copula . . . . .	26
4.2.4	Fatigue assessment . . . . .	28

4.3	Numerical integration procedures for mean damage estimation . . . . .	30
4.3.1	Quadrature rules and quasi-Monte Carlo methods . . . . .	30
4.3.2	Kernel discrepancy . . . . .	30
4.3.3	Kernel herding sampling . . . . .	33
4.3.4	Bayesian quadrature . . . . .	36
4.4	Numerical experiments . . . . .	39
4.4.1	Illustration through analytical toy-cases . . . . .	40
4.4.2	Application to the Teesside wind turbine fatigue estimation . . . . .	41
4.5	Conclusion . . . . .	44
<b>5</b>	<b>Kernel-based metamodel validation</b>	<b>47</b>
5.1	Introduction . . . . .	47
5.2	Sequential validation design . . . . .	47
5.3	Computer experiments context . . . . .	47
5.4	Machine learning given-data context . . . . .	47
5.5	Application to wind turbine production metamodel . . . . .	47
5.6	Conclusion . . . . .	47
<b>III</b>	<b>Contributions to rare event estimation</b>	<b>49</b>
<b>6</b>	<b>Nonparametric rare event estimation</b>	<b>51</b>
6.1	Introduction . . . . .	51
6.1.1	Background . . . . .	52
6.2	Bernstein adaptive nonparametric conditional sampling . . . . .	54
6.2.1	Empirical Bernstein copula . . . . .	54
6.2.2	Bernstein adaptive nonparametric conditional sampling algorithm	55
6.3	Numerical experiments . . . . .	58
6.3.1	Results analysis . . . . .	59
6.4	Application to wind turbine fatigue reliability . . . . .	59
6.5	Conclusion . . . . .	59
<b>7</b>	<b>Sequential reliability oriented sensitivity analysis</b>	<b>63</b>
7.1	Conclusion . . . . .	63
7.2	HSIC for GSA . . . . .	63
7.3	HSIC for TSA & CSA . . . . .	63
7.4	Sequential ROSA . . . . .	63
7.5	Application to wind turbine fatigue reliability . . . . .	63
7.6	Conclusion . . . . .	63
<b>Conclusion and perspectives</b>		<b>65</b>

<b>References</b>	<b>67</b>
<b>Appendix A Multivariate distribution modeling</b>	<b>73</b>
<b>Appendix B Nonparametric copula estimation</b>	<b>75</b>
<b>Appendix C Rare event estimation algorithms</b>	<b>77</b>
<b>Appendix D Résumé étendu de la thèse</b>	<b>79</b>

# List of figures

3.1	South Brittany wind farm layout (left). South Brittany wind rose from the ANEMOC data (right, source: [? ]). . . . .	14
3.2	Joint perturbation at WT 13, 19, and 25 . . . . .	16
3.3	Ambient and wake-disturbed distributions of the wind speed . . . . .	16
3.4	Ambient and wake-disturbed distributions of the turbulence intensity . . . . .	16
3.5	Kernel mean embedding of two probability distributions $P$ and $Q$ mapped in the RKHS $H_k$ . . . . .	17
3.6	South Brittany layout and wake effects measured by the squared MMD on wind conditions. Note that the vertical direction on this plot does not represent the north direction. . . . .	19
3.7	Convergence of the squared MMD estimation . . . . .	19
4.1	General uncertainty quantification and propagation framework (adapted from [2]) . . . . .	22
4.2	Diagram of the chained OWT simulation model . . . . .	23
4.3	Teesside wind farm layout (left). Monopile OWT diagram [11] (right) . . . . .	24
4.4	Copulogram of the Teesside measured data ( $N = 10^4$ in grey), kernel herding subsample ( $n = 500$ in orange). Marginals are represented by univariate kernel density estimation plots (diagonal), the dependence structure with scatter plots in the ranked space (upper triangle). Scatter plots on the bottom triangle are set in the physical space . . . . .	27
4.5	Angular distribution of the wind and waves with a horizontal cross-section of the OWT structure and the mudline . . . . .	29
4.6	Histogram of the log-damage, at mudline, azimuth 45 deg. (Monte Carlo reference sample) . . . . .	29
4.7	Kernel mean embedding of a continuous and discrete probability distribution . . . . .	32
4.8	Kernel illustrations (left to right: energy-distance, squared exponential, and Matérn 5/2) . . . . .	35
4.9	Sequential kernel herding for increasing design sizes ( $n \in \{10, 20, 40\}$ ) built on a candidate set of $N = 8196$ points drawn from a complex Gaussian mixture $\mu$ . . . . .	36

4.10	Bayesian quadrature on a one-dimensional case . . . . .	38
4.11	Analytical benchmark results on the toy-case #1 . . . . .	42
4.12	Analytical benchmark results on the toy-case #2 . . . . .	43
4.13	Sampling techniques used for the industrial use case . . . . .	44
4.14	Copulogram of the kernel herding design of experiments with corresponding outputs in color (log-scale) on the Teesside case ( $n = 10^3$ ). The highest values are in red while the lowest values are in blue. Marginals are represented by histograms (diagonal), the dependence structure with scatter plots in the ranked space (upper triangle). Scatter plots on the bottom triangle are set in the physical space. . . . .	45
4.15	Mean estimation convergence (at the mudline, azimuth $\theta = 45$ deg.) on the Teesside case . . . . .	46
6.1	Evolution of $m_{\text{IMSE}}$ for different dimensions and sample sizes. . . . .	55
6.2	BANCS on toy-case #1: illustration of conditional sampling and nonparametric fit at the first and second iterations. . . . .	56
6.3	QQ-plot for KDE of marginals of the conditional distribution from Fig. 6.2.	57
6.4	Kendall plot for EBC on the copula of a conditional distribution from Fig. 6.2.	57
6.5	BANCS sampling steps on toy-case #1. . . . .	60
6.6	BANCS sampling steps on toy-case #2. . . . .	60

# List of tables

4.1	Teesside Offshore Wind turbine datasheet . . . . .	23
4.2	Description of the environmental data. . . . .	26
4.3	Kernels considered in the following numerical experiments. . . . .	35
4.4	Analytical toy-cases . . . . .	41
6.1	Results of the numerical experiments (subset sample size $N = 10^4$ , $p_0 = 0.1$ ). .	59



# **Introduction**

## **Context**

**General methodology for treatment of uncertainties**

## **Problem statement**

**Objectives and outline of the thesis**

## **Problem statement**

[21]

## Publications and communications

The research contributions in this manuscript are based on the following publications:

- Book Chap. [E. Fekhari](#), B. Iooss, J. Muré, L. Pronzato and M.J. Rendas (2023). “Model predictivity assessment: incremental test-set selection and accuracy evaluation”. In: *Studies in Theoretical and Applied Statistics*, pages 315–347. Springer.
- Jour Pap. [E. Fekhari](#), V. Chabridon, J. Muré and B. Iooss (2023). “Fast given-data uncertainty propagation in offshore wind turbine simulator using Bayesian quadrature”. In: *Data-Centric Engineering*.
- Int. Conf [E. Fekhari](#), B. Iooss, V. Chabridon, J. Muré (2022). “Numerical Studies of Bayesian Quadrature Applied to Offshore Wind Turbine Load Estimation”. In: *SIAM Conference on Uncertainty Quantification (SIAM UQ22)*, Atlanta, USA. (Talk)
- [E. Fekhari](#), B. Iooss, V. Chabridon, J. Muré (2022). “Model predictivity assessment: incremental test-set selection and accuracy evaluation”. In: *22nd Annual Conference of the European Network for Business and Industrial Statistics (ENBIS 2022)*, Trondheim, Norway. (Talk)
- [E. Fekhari](#), B. Iooss, V. Chabridon, J. Muré (2022). “Efficient techniques for fast uncertainty propagation in an offshore wind turbine multi-physics simulation tool”. In: *Proceedings of the 5th International Conference on Renewable Energies Offshore (RENEW 2022)*, Lisbon, Portugal. (Paper & Talk)
- [E. Fekhari](#), V. Chabridon, J. Muré and B. Iooss (2023). “Bernstein adaptive nonparametric conditional sampling: a new method for rare event probability estimation”. In: *Proceedings of the 13th International Conference on Applications of Statistics and Probability in Civil Engineering (ICASP 14)*, Dublin, Ireland. (Paper & Talk)
- E. Vanem, [E. Fekhari](#), N. Dimitrov, M. Kelly, A. Cousin and M. Guiton (2023). “A joint probability distribution model for multivariate wind and wave conditions”. In: *Proceedings of the ASME 2023 42th International Conference on Ocean, Offshore and Arctic Engineering (OMAE 2023)*, Melbourne, Australia. (Paper)
- A. Lovera, [E. Fekhari](#), B. Jézéquel, M. Dupoirion, M. Guiton and E. Ardillon (2023). “Quantifying and clustering the wake-induced perturbations within a wind farm for load analysis”. In: *Journal of Physics: Conference Series (WAKE 2023)*, Visby, Sweden (Paper)
- Nat. Conf. [E. Fekhari](#), B. Iooss, V. Chabridon, J. Muré (2022). “Kernel-based quadrature applied to offshore wind turbine damage estimation”. In: *Proceedings of the Mascot-Num 2022 Annual Conference (MASCOT NUM 2022)*, Clermont-Ferrand, France (Poster)
- [E. Fekhari](#), B. Iooss, V. Chabridon, J. Muré (2023). “Rare event estimation using nonparametric Bernstein adaptive sampling”. In: *Proceedings of the Mascot-Num 2023 Annual Conference (MASCOT-NUM 2023)*, Le Croisic, France (Talk)

## **Part I**

# **Introduction to treatment of uncertainties and wind energy**



# Chapter 1

## Treatment of uncertainties in computer experiments

### 1.1 Introduction

### 1.2 Problem specification (step A)

#### 1.2.1 Black-box computer model

#### 1.2.2 Output quantity of interest

### 1.3 Input uncertainty quantification (step B)

#### 1.3.1 Joint probability distribution [copulogram package]

#### 1.3.2 Parametric multivariate estimation

#### 1.3.3 Non-parametric multivariate estimation

#### 1.3.4 Goodness-of-fit

### 1.4 Uncertainty propagation for central tendency estimation (step C)

#### 1.4.1 Numerical integration

“Good” properties

[Curse of dim / Sequential / Deterministic]

Gauss-Kronrod

Monte Carlo

Quasi-Monte Carlo and Koksma-Hlawka inequality

### 1.4.2 Numerical design of experiments

Space-filling metrics

[MinMax / PhiP / MaxMin / Discrepancies]

“Good” properties

[Curse of dim / Projections in sub-spaces / Sequential / Deterministic]

Monte Carlo, quasi-Monte Carlo, randomized quasi-Monte Carlo designs

LHS, optimized LHS designs

### 1.4.3 Central tendency estimation

Iso-probabilistic transformation

Central tendency estimation is a probabilistic integration

## 1.5 Uncertainty propagation for rare event estimation (step C)

### 1.5.1 Problem formalization

Limit-state function, failure event and domain

Risk measures [Failure probability, quantile, super-quantile]

### 1.5.2 Rare event estimation methods

FORM/SORM

Monte Carlo

Importance sampling

Adaptive sampling (SS/NAIS/IS-CE/Moving particles)

## 1.6 Sensitivity analysis (step C')

### 1.6.1 Global sensitivity analysis

### 1.6.2 Reliability-oriented sensitivity analysis

## 1.7 Metamodeling

### 1.7.1 Global metamodel

### 1.7.2 Reliability-oriented metamodel

## 1.8 Conclusion





# Chapter 2

## Introduction to wind turbine modeling and design

### 2.1 Introduction

### 2.2 Wind turbine modeling

#### 2.2.1 Synthetic wind generation [**TurbSim, Kaimal spectrum**]

#### 2.2.2 Synthetic wave generation

#### 2.2.3 Aerodynamic interactions

#### 2.2.4 Servo-Hydro-Aero-Elastic wind turbine simulation [**DIEGO**]

#### 2.2.5 Soil modeling

#### 2.2.6 Wake modeling [**FarmShadow**]

### 2.3 Recommended design practices

#### 2.3.1 Design load cases

#### 2.3.2 Dynamic response design

#### 2.3.3 Fatigue response design

### 2.4 Uncertain inputs

#### 2.4.1 Environmental inputs

#### 2.4.2 System inputs

#### 2.4.3 Probabilistic fatigue assessment

### 2.5 Conclusion

## **Part II**

# **Contributions to uncertainty quantification and propagation**



# Chapter 3

## Kernel-based uncertainty quantification

### 3.1 Introduction

### 3.2 Nonparametric fit of the environmental inputs

### 3.3 Quantifying and clustering the wake-induced perturbations within a wind farm

In the offshore wind industry, the wake effect is considered crucial for electricity production and structural fatigue of turbine components. For instance, the standards developed by the International Electrotechnical Commission (see appendix E in [? ]) review some analytical [? ], and numerical models (e.g., the dynamic wake meandering approach by [? ]) to simulate the wind speed deficit and the wake added turbulence. Since the pioneering work of [? ], several wake models were developed and compared in a benchmark by [? ]. This work takes advantage of the low computational cost of steady-state wake models to propagate the uncertainty from ambient to wake-induced wind conditions seen on a farm. It is worth noting that the wake creates a heterogeneous wind field in a wind farm, resulting in different loading conditions which should be considered at the stage of reliability based design (RBD). Such heterogeneity is not taken into account by the design load cases of international standards (see e.g., [? ? ]) where wind and wave conditions are derived from scenarios occurring over long-term periods. Wake models allow us to simulate the wind conditions' distribution at each turbine, however, the RBD step is too costly to be performed for each turbine. For further details regarding the RBD, one may refer to the work of [27, 71, 73, 80], proposing several approaches to reduce the computational cost of this step. In order to speed up the RBD at the scale of a wind farm, the present work aims at building clusters of WT similarly affected by the wake. Then, the RBD over a wind farm can be computed only on a few WT, each representing a cluster of turbines enduring similar wake-modified wind loading. This clustering is done on two wind parameters, following

the conclusions of the global sensitivity analysis of [? ]. In order to discriminate the wake-perturbed distributions of wind parameters, the maximum mean discrepancy (MMD) is used as a statistical metric between multivariate distributions (as reviewed by [? ]). To illustrate this novel approach, a theoretical wind farm for the ongoing tenders off the coast of South Brittany in France is studied, with a modified version of the floating offshore wind turbine (FOWT) IEA-15MW (initially proposed in [? ? ]). Figure 3.1 illustrates the layout of the 25 FOWT considered in the following. This layout is regular with an inter-turbine distance of seven times the rotor diameter in the dominant wind direction and five times the rotor diameter in the orthogonal (crosswind) direction. More details regarding the FOWT modifications and theoretical wind farm can be found in [? ? ].

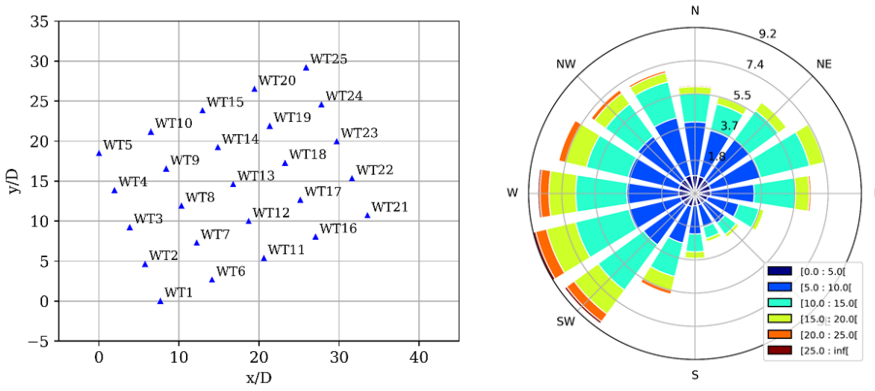


Fig. 3.1 South Brittany wind farm layout (left). South Brittany wind rose from the ANEMOC data (right, source: [? ]).

Based on the results of previous numerical studies, with either dynamic wake meandering [?] or LES [? ], we retain the time-averaged floater position (translation and rotation) as the main effect of the floater motion on the far wake. It was shown that this effect is small, both on the wake-added turbulence and on the wind speed deficit. However, noticeable uplift of the wake may influence the fatigue design.

The key idea in this paper to reduce the number of cases for RBD is to employ clustering techniques on the wake-induced wind parameters, to constitute groups of WT that are exposed to similar design load conditions. To do so, the present work is divided into four sections. First, the wake model used in this work is presented in section ???. Then, section 3.3.1 describes the uncertainty propagation through the wake model, from the probabilistic distribution of ambient wind parameters to the wake-modified wind parameters distribution within the farm. In order to regroup the similar wake-modified distributions, an adapted statistical metric on multivariate distributions is introduced in section 3.3.2. Finally, the application of several clustering methods to the South Brittany case study is compared in section ???. The main conclusion suggests four clusters among the 25 FOWT which can then be used for RBD analysis of the farm.

### 3.3.1 Uncertainty propagation in a wake model

The wake model described in section ?? takes as input a set of variables describing the ambient wind conditions  $\mathbf{x} \in \mathbb{R}^3$  and computes the perturbed wind conditions at each WT represented by the vector  $\mathbf{x}'_l, l \in (1, \dots, n_{WT})$ , where  $n_{WT}$  is the total number of turbines in the farm:

$$g : \mathbb{R}^3 \rightarrow \mathbb{R}^{3n_{WT}} \quad (3.1)$$

$$\mathbf{x} \longmapsto g(\mathbf{x}) = (\mathbf{x}'_1, \dots, \mathbf{x}'_{n_{WT}}) \quad (3.2)$$

The uncertainties associated with the ambient wind conditions are represented by a random vector  $\mathbf{X}$  following the distribution  $p_0$ . Note that the index 0 is a reference to the fact that these conditions are not perturbed by the wake. A parametric model has been fitted in [77] using conditional probability density functions to capture the dependence structure, with an approach similar to the one presented in [38]. The random vector  $\mathbf{X}$  is described by the following input random variables:

- Mean wind speed ( $u$ ) is the 10-min average horizontal wind speed at hub height.
- Wind turbulence intensity ( $TI$ ) is the 10-min wind speed turbulence intensity at hub height.
- Wind direction ( $\theta$ ) is the 10-min average wind direction.

In the following, we assume the wind orientation variable  $\theta$  to be unaffected by the wake. When perturbed by the wake of the wind farm, the WT  $l$  sees a wind flow represented by the random vector  $\mathbf{X}'_l, l \in (1, \dots, n_{WT})$ , following the distribution  $p'_l$ . Then, the two remaining parameters are  $u_{rotor}$  and  $TI_{rotor}$  to represent this modified wind flow on a vertical plane located at each WT. These two quantities of interest are averaged over the rotor while the input parameters are given at hub height. For the sake of simplicity, we will neglect this difference in what follows in order to consider the transformation  $\mathbf{X}' = g(\mathbf{X})$  as a simple perturbation of  $\mathbf{X}$ . We will abusively denote  $u$  and  $TI$  both the input and output quantities. The output of the uncertainty propagation is a set of perturbed environmental distributions  $p'_l, l \in (1, \dots, n_{WT})$ . A Monte-Carlo sample  $\mathbf{X}_n = \mathbf{x}^{(1)}, \dots, \mathbf{x}^{(n)}$  of the three random input variables is generated. Then, considering the farm layout illustrated in Figure 3.1 and a constant wind shear exponent of 0.1 like in section ??, a wake simulation is run for every wind condition of the Monte Carlo design of experiments. The code output consists in a multivariate joint distribution of modified  $u$  and  $TI$  for each WT. As the Monte Carlo procedure is known to converge slowly but surely, it was chosen to perform this uncertainty propagation with a number of simulations of size  $n = 6\,000$  because of its simplicity and the low computational cost of the simulations.

We can plot a preview of the wake perturbations on the joint distribution for given WT in the two dimensions  $u$  and  $TI$ . Figure 3.2 illustrates this perturbation for three WT

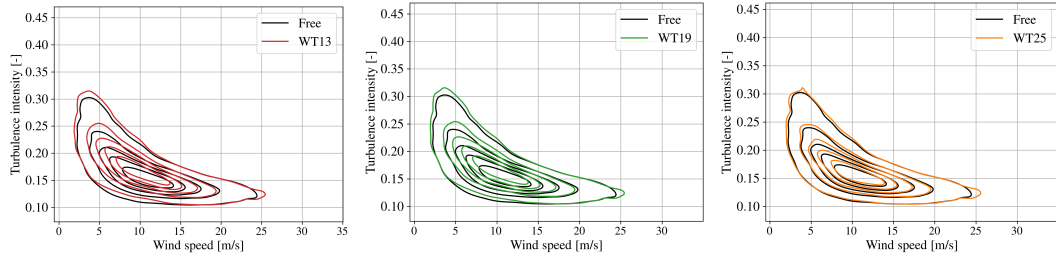


Fig. 3.2 Joint perturbation at WT 13, 19, and 25

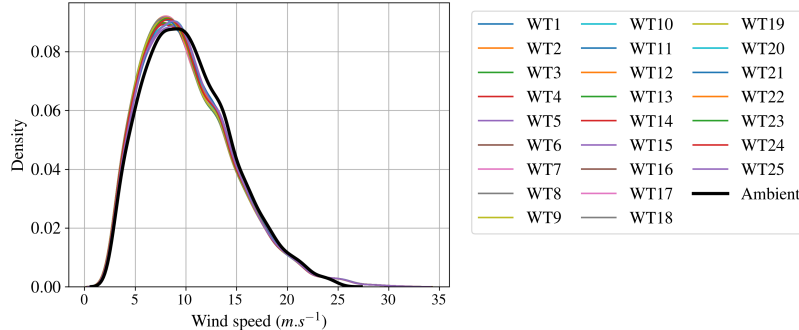


Fig. 3.3 Ambient and wake-disturbed distributions of the wind speed

differently affected by the wake depending on their position in the farm (cf. Figure 3.1). One can notice that the WT 25 distribution (in orange) is very close to the ambient distribution (in black), as expected, this WT being located on the edge of the farm and facing the dominant wind direction. Meanwhile, the WT 13 distribution (in red) seems more affected by the wake, by getting a higher wind turbulence with lower wind speed. This analysis can be completed with the two marginals in Figure 3.3 and Figure 3.4, both describing the ambient marginal distributions (in black) and wake-disturbed distributions. In general, a small wind speed deficit is noticed as indicated by the small shifts of the probability density functions to the left on Figure 3.3. Also, a small added turbulence is indicated by the small shifts of the curves to the right on Figure 3.4. Ideally, a tool should allow us to quantify the perturbation between the ambient and perturbed distributions.

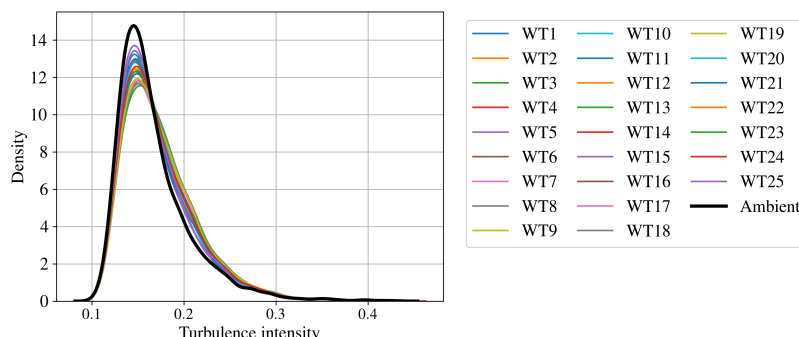


Fig. 3.4 Ambient and wake-disturbed distributions of the turbulence intensity

### 3.3.2 Statistical metric of wake-induced perturbations

**Maximum mean discrepancy: a distance between distributions** In the literature, the maximum mean discrepancy was introduced by [25] as a statistical test to discriminate two distinct distributions. After further work on this tool, authors such as [72] showed that the MMD is a distance between two distributions embedded in a specific function space. Therefore, this concept relies on the embedding of distributions in a convenient Hilbert space. Considering a positive-definite kernel  $k : \mathbb{R}^d \times \mathbb{R}^d \rightarrow \mathbb{R}, d \in \mathbb{N}$  generating a unique Hilbert space  $\mathcal{H}_k$  of functions equipped with inner products  $\langle \cdot, \cdot \rangle_{\mathcal{H}_k}$  and norms  $\|\cdot\|_{\mathcal{H}_k}$  (also called Reproducing Kernel Hilbert Space (RKHS) when the function  $k(\mathbf{x}, \cdot)$  satisfies the reproducing property). Then, let us define the kernel mean embedding of the distribution  $P$  in the function space  $\mathcal{H}_k$ :

$$\mu_P(\mathbf{x}) := \int_{\mathbb{R}^d} k(\mathbf{x}, \mathbf{y}) dP(\mathbf{y}) \approx \frac{1}{n} \sum_{i=1}^n k(\mathbf{x}, \mathbf{x}^{(i)}), \mathbf{x}^{(i)} \in \mathbf{X}_n. \quad (3.3)$$

The kernel mean embedding is approximated on sample  $\mathbf{X}_n = (\mathbf{x}^{(1)}, \dots, \mathbf{x}^{(n)})$  following the distribution  $P$ . Figure 3.5 illustrates the kernel mean embedding of two distributions in the function space  $\mathcal{H}_k$  defined previously. Notice that this procedure allows us to embed continuous distributions (such as  $P$ ) as well as discrete distributions (such as  $Q$ ).

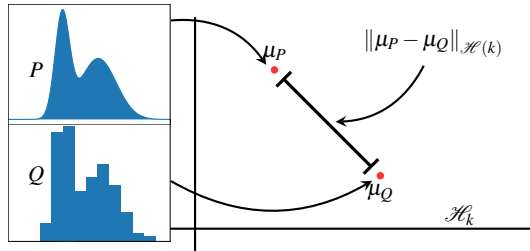


Fig. 3.5 Kernel mean embedding of two probability distributions  $P$  and  $Q$  mapped in the RKHS  $H_k$

The distance between the two kernel mean embeddings  $\mu_P$  and  $\mu_Q$  is called the maximum mean discrepancy (MMD). This distance between two distributions  $P$  and  $Q$  is initially defined by the worst-case error for any function within a unit ball of a Hilbert space  $\mathcal{H}_k$ , generated by the kernel  $k$ :

$$\text{MMD}_k(P, Q) := \sup_{\|g\|_{\mathcal{H}_k} \leq 1} \left| \int_{\mathbb{R}^d} g(\mathbf{x}) dP(\mathbf{x}) - \int_{\mathbb{R}^d} g(\mathbf{x}) dQ(\mathbf{x}) \right| = \|\mu_P(\mathbf{x}) - \mu_Q(\mathbf{x})\|_{\mathcal{H}_k}. \quad (3.4)$$

The MMD fully relies on the difference of kernel mean embeddings. Moreover, according to [72], a kernel is called “characteristic kernel” when the following equivalence is true,  $\text{MMD}_k(P, Q) = 0 \iff P = Q$ , making the MMD a metric on  $\mathbb{R}^d$ . For its good convergence

behavior, the squared MMD has been used for multiple other purposes than numerical integration: statistical testing [25], sensitivity analysis [13]. When elevated to the square, it can be estimated using one  $n$ -sized representative sample of  $P$  denoted  $\{\mathbf{x}^{(i)}\}_{i \in (1, \dots, n)}$  (and respectively one  $m$ -sized sample of  $Q$  denoted  $\{\mathbf{y}^{(i)}\}_{i \in (1, \dots, m)}$ :

$$\widehat{\text{MMD}}_k(P, Q)^2 = \frac{1}{n^2} \sum_{i,j=1}^n k(\mathbf{x}^{(i)}, \mathbf{x}^{(j)}) - \frac{2}{nm} \sum_{i=1}^n \sum_{j=1}^m k(\mathbf{x}^{(i)}, \mathbf{y}^{(j)}) + \frac{1}{m^2} \sum_{i,j=1}^m k(\mathbf{y}^{(i)}, \mathbf{y}^{(j)}). \quad (3.5)$$

In the following, the idea is to compare the ambient wind distribution  $p_0$  to the wake-perturbed wind conditions  $p'_l$  at the WT  $l$  using the previously defined squared MMD.

**Application to the South Brittany wind farm project** Once the joint perturbed distributions of each WT are estimated by a large Monte Carlo sample (cf. section 3.3.1), the MMD with the ambient wind conditions can be computed. Figure 3.6 illustrates for each WT the squared MMD value computed to measure the wake-induced perturbation. Let us remind that MMD is a distance between the joint perturbed distribution at a WT computed for all wind orientations with the ambient wind distribution. Despite the wake obviously depend on the wind direction, our final goal is to define a small number of WT for RBD thus independently of the wind orientation. The lower this metric gets, the closer to the ambient wind distribution. Quite logically, the WT in the center of the farm are more affected by the wake since they are subject to the wake regardless of the wind direction.

The values of squared MMD given in the previous figure are estimated between two samples:

- the Monte Carlo sample of the free environmental distribution:  $\mathbf{X}_n$ ,
- the wake-perturbed Monte Carlo sample at the WT  $l$ :  $\mathbf{X}'_{n,l}$  (output of the steady-state wake numerical model).

To ensure that the Monte-Carlo estimation converged, Figure 3.7 plots the squared MMD between the sample  $\mathbf{X}_n$  and the increasing samples  $\mathbf{X}'_{i,l}, i \in 400, \dots, 6000$ . After a few thousands of simulations, the MMD of each WT tends to converge towards a stable value, as expected. The design of experiment with  $n = 6\,000$  is thus considered as sufficient.

### 3.3.3 Conclusion

A steady-state engineering wake model is coupled with a hydrostatic solver to take into account the effect of the floaters position in the wake computation of a floating offshore wind farm. The main impact of the floater's position is the increased rotor tilt, which leads to a larger vertical deflection of the wake. In the South-Brittany farm, the elevation of wake center is significant and could modify the fatigue loads on the downstream WT. This

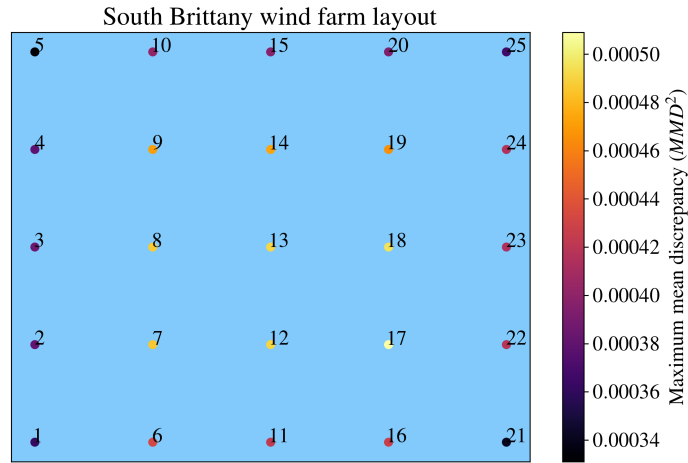


Fig. 3.6 South Brittany layout and wake effects measured by the squared MMD on wind conditions. Note that the vertical direction on this plot does not represent the north direction.

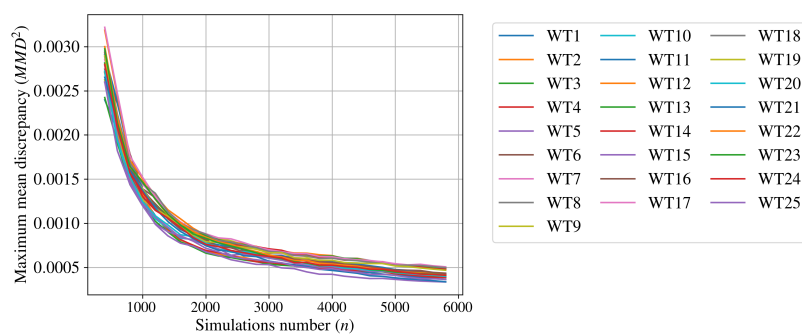


Fig. 3.7 Convergence of the squared MMD estimation

low-fidelity, or engineering model is very fast (about 3 minutes on a regular computer), while higher fidelity models can simulate the wake in a wind farm more accurately, but with much higher computational cost (several days for LES Meso-NH solver, with intensive parallelisation). In this paper, we consider that the modelling error made by the engineering wake model is reasonable. Further investigations should be done on the integration of the different fidelity levels in the uncertainty propagation. In this work, the uncertainty propagation is performed for random inputs: the wind speed and the turbulence intensity, leading to a wake perturbed distribution per WT. A metric was then defined to measure the distance between distributions in order to build clusters of WT seeing similar wind conditions. After applying the metric to the South Brittany case, a clustering approach is used to determine a limited number of WTs representing the farm for RBD. Several clustering methods are compared and provide similar results for the current case study. In this case, a solution with 4 clusters is a good compromise between low relative error with clusters and low number of clusters. Getting a low number of clusters allows us to reduce the number of representative WT on which a RBD study can be done to assess the RBD over the whole farm. The differences among a cluster and between clusters have to be studied when looking directly to the output of interest for ultimate or fatigue reliability. However the difference on load output quantities may be reduced when compared to that on wake output quantities thanks to the damping of the WT. Depending on the definition of a wind farm failure (series system: one WT fails or parallel system: all WT fail or intermediate system), the probability of failure can be estimated from the probability of failure of the representative WT. These considerations need to be further explored to improve RBD at the farm scale.

### 3.4 Conclusion

# Chapter 4

## Kernel-based central tendency estimation

### 4.1 Introduction

As a sustainable and renewable energy source, offshore wind turbines (OWT) are likely to take a growing share of the global electric mix. However, to be more cost-effective, wind farm projects tend to move further from the coast, exploiting stronger and more regular wind resources. Going further offshore, wind turbines are subject to more severe and uncertain environmental conditions (i.e., wind and waves). In such conditions, their structural integrity should be certified. To do so, numerical simulation and probabilistic tools have to be used. In fact, according to [24], for new environmental conditions or new turbine models, international standards such as [30] from the International Electrotechnical Commission and [18] from Det Norske Veritas recommend performing over 200,000 simulations distributed over a grid. Numerical simulations are computed by a costly hydro-servo-aero-elastic wind turbine model, making the design process time-consuming. In the following, the simulated output cyclic loads studied are aggregated over the simulation period to assess the mechanical fatigue damage at hot spots of the structure. To compute the risks associated with wind turbines throughout their lifespan, one can follow the steps of the universal framework for the treatment of uncertainties [15] presented in Fig. 4.1. After defining the problem (Step A), one can quantify the uncertainties related to site-specific environmental conditions denoted by the random variable  $\mathbf{X}$  (Step B). Then, one can propagate them through an OWT simulation model  $g(\cdot)$  (Step C), and estimate a relevant quantity of interest  $\psi(Y) = \psi(g(\mathbf{X}))$  (e.g., mean, quantile, failure probability). A proper estimation of the quantity relies on a good uncertainty model and an efficient sampling method to estimate the quantity of interest.

The uncertainties related to the OWT environment follow a joint distribution with a complex dependence structure. This challenging distribution has been fitted with different parametric approaches in the literature (step B in Fig. 4.1), mainly using conditional distributions [77], but also vine copulas [48]. When one has access to data, another way is to directly use the data as empirical representation of input uncertainties.

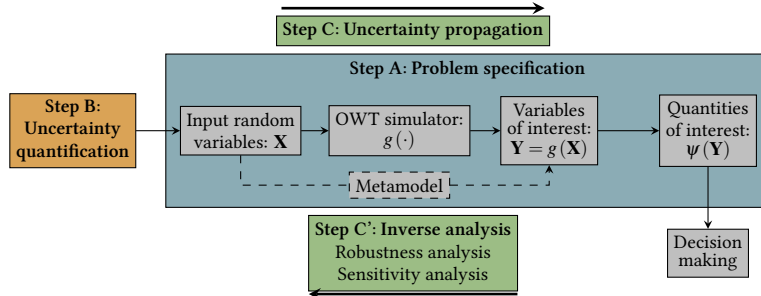


Fig. 4.1 General uncertainty quantification and propagation framework (adapted from [2])

These uncertainties have then been propagated to fatigue damage (the output), making it random, and to the associated quantities of interest (step C in Fig. 4.1). When uncertainty propagation aims at central tendency studies, the methods employed are split into two groups. Methods of the first group rely on numerical integration by Monte Carlo sampling [24], quasi-Monte Carlo sampling [57], or deterministic quadrature rules [76]. All these methods estimate the quantity directly on the numerical simulator's outputs. Methods of the second group use metamodels (or surrogate models) to emulate the costly numerical model by a statistical model such as polynomial chaos expansion [16, 56], Gaussian processes [27, 71, 80], or artificial neural networks [4].

When uncertainty propagation aims at studying the tail of the output distribution (e.g., reliability analysis), one can estimate a quantile or a failure probability. Failure probabilities were studied, in static reliability analysis [82, 71, 80] or time-dependent reliability analysis [1, 45]. To get a better understanding of the OWT numerical models behavior, authors have used sensitivity analysis methods [14], which determine the most influential inputs on the damage (step C' in Fig. 4.1). Among others, one can cite the application of Spearman's rank correlation coefficients and Morris method's by [78, 63], the direct calculation of Sobol' indices after fitting a polynomial chaos model by [56] and the use of Kullback-Leibler divergence by [75]. Each of those methods brings something different to the analysis.

This paper will focus on central tendency estimation (i.e.,  $\psi(\mathbf{X}) = \mathbb{E}(\mathbf{X})$ ) by: (1) direct sampling on the numerical model, (2) sampling on a static regression model, or (3) sampling on an active regression model (i.e., observations of the numerical model are progressively added to enhance a goal-oriented metamodel). In the specific context of wind turbines, this paper explores how to study the central tendency study of the fatigue damage output, by carrying out the uncertainty propagation of a complex input joint distribution through a costly wind turbine simulator. This work proposes a new approach for given data, fast, and fully-distributable uncertainty propagation for OWT models. Overall, this paper reviews the methods of Bayesian quadrature and presents its application on the industrial wind turbines case. In this paper, Section 2 will detail the industrial use-case related to a wind farm operating in Teesside, UK. Then, Section 3 will introduce different methods for central tendency estimation. Section 4 will analyze the results of numerical experiments

on analytical and industrial cases. Then, the last section will present discussions and conclusions.

## 4.2 Treatment of uncertainties on the Teesside wind farm

An OWT is a complex system interacting with its environment. To simulate the response of this system against a set of environmental solicitations, multi-physics numerical models are developed. In our case, it is a chain of three numerical codes executed sequentially. As illustrated in Fig. 4.2, a simulation over a time period is the sequence of (1) turbulent wind speed field generation, (2) wind turbine simulation (computing various outputs including mechanical stress), and (3) post-processing to assess the fatigue damage of the structure.

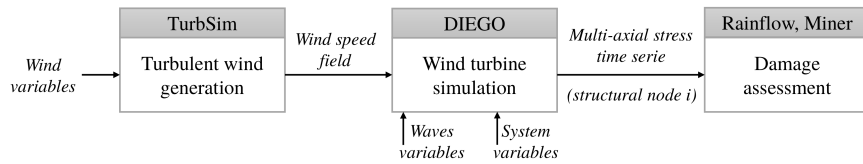


Fig. 4.2 Diagram of the chained OWT simulation model

Table 4.1 Teesside Offshore Wind turbine datasheet

Siemens SWT-2.3-93	
Rated power	2.3 MW
Rotor diameter	93 m
Hub height	83 m
Cut-in, cut-out wind speed	4 m/s, 25 m/s

### 4.2.1 Numerical simulation model

This section describes more precisely the modeling hypotheses considered in this case. Starting from the turbulent wind field simulator TurbSim (developed by [33] from the National Renewable Energy Laboratory, USA) that uses a Kaimal spectrum [34]. To extrapolate the wind speed vertically, the shear is modeled by a power law. Since the wind field generation shows inherent stochasticity, each 10-minute long simulation is repeated with different pseudo-random seeds and the average damage over these repetitions is studied. This question was widely studied by some authors, (e.g., [71]), who concluded that the six repetitions recommended by the [30] are insufficient to properly average this stochasticity. In the following, the simulations are repeated eleven times (allowing direct access to the median value). This number of repetitions was chosen as a compromise between the general number of simulations and the storage capacity of the generated simulations.

DIEGO (for “Dynamique Intégrée des Éoliennes et Génératrices Offshore<sup>1</sup>”) is a code developed by EDF R&D [39] to simulate the aero-hydro-servo-elastic behavior of OWTs. It takes the turbulent wind speed field generated by TurbSim as input and computes the dynamical behavior of the system (including the multiaxial mechanical stress at different nodes of the structure). For our application, the control system is modeled by the open-source DTU controller [26], and no misalignment between the wind and the OWT is assumed. As for the waves, they are modeled in DIEGO using a JONSWAP spectrum (named after the 1975 Joint North Sea Wave Project). Our study uses a DIEGO model of a Siemens SWT 2.3MW bottom-fixed turbine on a monopile foundation (see the datasheet in Table 4.1), currently operating in Teesside, UK (see the wind farm layout and wind turbine diagram in Fig. 4.3). Although wind farms are subject to the wake effect, affecting the behavior and performance of some turbines in the farm, this phenomenon is not considered in the following. To avoid numerical perturbations and reach the stability of the dynamical system, our simulation period is extended to 1000 seconds and the first 400 seconds are cropped in the post-processing step. This chained OWT numerical simulation model has been deployed on an EDF R&D HPC facility to benefit from parallel computing speed up (a single simulation on one CPU takes around 20 minutes).

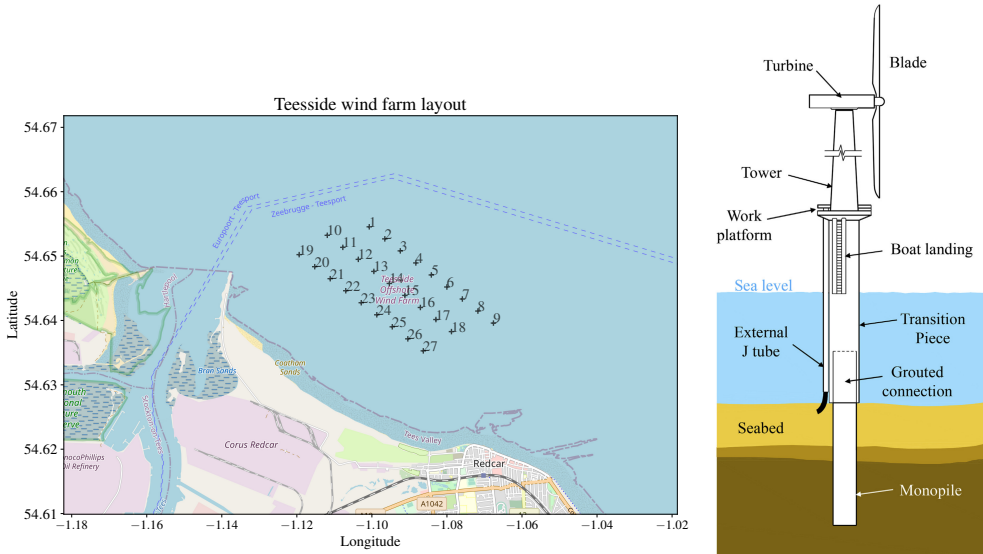


Fig. 4.3 Teesside wind farm layout (left). Monopile OWT diagram [11] (right)

#### 4.2.2 Measured environmental data

During the lifespan of a wind farm project, environmental data is collected at different phases. In order to decide on the construction of a wind farm, meteorological masts and wave buoys are usually installed on a potential site for a few years. After its construction,

<sup>1</sup>In english, “Integrated Dynamics of Wind Turbines and Offshore Generators”.

each wind turbine is equipped with monitoring instruments (e.g., cup anemometers). In total, five years of wind data have been collected on the turbines which are not affected by the wake on this site. Their acquisition system (usually called SCADA, for “Supervisory Control And Data Acquisition”) have a sampling period of ten minutes. The wave data arise from a buoy placed in the middle of the farm. This data describes the physical features listed in Table 4.2.

The farm of Teesside is located close to the coast, making the environmental conditions very different depending on the direction (see the wind farm layout in Fig. 4.3). Since measures are also subject to uncertainties, a few checks were realized to ensure that the data were physically consistent. The truncation bounds defined in Table 4.2 were applied since this study is not interested in extreme values but central tendency estimation (i.e., mean behavior). In addition, a simple trigonometric transform is applied to each directional feature to take into account their cyclic structure. Finally, the remaining features are rescaled (i.e., using a min-max normalization). The matrix plot of the transformed data in Fig. 4.4 is an innovative plot named *copulogram*. A copulogram is an innovative plot as it decomposes the data between the effects of the marginals and those of the dependence between features. To do so, it represents the marginals with univariate kernel density estimation plots (diagonal), and the dependence structure with scatter plots in the ranked space (upper triangle). On the bottom triangle the scatter plots are set in the physical space, gathering the effects of the marginals and the dependencies. Since the dependence structure is theoretically modeled by an underlying copula, this plot is called *copulogram*, generalizing the well-known “correlogram” to nonlinear dependencies. It gives a synthetic and empirical decomposition of the dataset.

On Fig. 4.4, a large sample  $\mathcal{S}$  (with a size  $N = 10^4$ ) is randomly drawn from the entire Teesside data (with size  $N_{\text{Teesside}} = 2 \times 10^5$ ), and plotted in grey. In the same figure, the orange matrix plot is a subsample of the sample  $\mathcal{S}$ , selected by kernel herding, a method that will be presented in Section 3. Visually, this orange subsample seems to match the original sample both in terms of marginal distributions and dependence structure. In the following study, the large samples  $\mathcal{S}$  will be considered as an empirical representation of the multivariate environmental distribution  $\mathbf{X} \in \mathcal{D}_{\mathbf{X}} \subset \mathbb{R}^p$ , of density  $f_{\mathbf{X}}$ , and called *candidate set*. Contrarily to parametric approaches which can be used to describe the joint environmental uncertainty, this method intends to directly subsample from this large and representative dataset. This technique samples a joint distribution without modeling it. Indeed, a proper parametric model fit would be challenging for complex dependence structures such as the one plotted on Fig. 4.4. [48] built a parametric model of a similar multivariate distribution using vine copulas. Alternatively, a nonparametric approach coupling empirical Bernstein copula fitting with kernel density estimation of the marginals is introduced in Section 4.2.3.

Table 4.2 Description of the environmental data.

Variable	Notation	Unit	Description
Mean wind speed	$U$	$\text{m.s}^{-1}$	10-min. average horizontal wind speed
Wind turbulence	$\sigma_U$	$\text{m.s}^{-1}$	10-min. wind speed standard deviation
Wind direction	$\theta_{wind}$	deg.	10-min. average wind direction
Significant wave height	$H_s$	m	Significant wave height
Peak wave period	$T_p$	s	Peak 1-hour spectral wave period
Wave direction	$\theta_{wave}$	deg.	10-min. average wave direction

#### 4.2.3 Non parametric fit with empirical Bernstein copula

The Sklar theorem [31] states that the multivariate distribution of any random vector  $\mathbf{X} \in \mathbb{R}^p$  can be broken down into two objects:

1. A set of univariate marginal distributions to describe the behavior of the individual variables;
2. A function describing the dependence structure between all variables, called a copula.

This theorem states that considering a random vector  $\mathbf{X} \in \mathbb{R}^p$ , with its distribution  $F$  and its marginals  $\{F_i\}_{i=1}^p$ , there exists a copula  $C : [0, 1]^p \rightarrow [0, 1]$ , such that:

$$F(x_1, \dots, x_p) = C(F_1(x_1), \dots, F_p(x_p)). \quad (4.1)$$

It allows us to divide the problem of fitting a joint distribution into two independent problems: fitting the marginals and fitting the copula. Additionally, when the joint distribution is continuous, this copula is unique. Copulas are continuous and bounded functions defined on a compact set (the unit hypercube). Bernstein polynomials allow to uniformly approximate as closely as desired any continuous and real-valued function defined on a compact set (Weierstrass approximation theorem). Therefore, they are good candidates to approximate unknown copulas. This concept was introduced as *empirical Bernstein copula* (EBC) by [68] for applications in economics and risk management. Later on, [69] offered further asymptotic studies. Formally, the multivariate Bernstein polynomial for a function  $C : [0, 1]^p \rightarrow \mathbb{R}$  on a grid over the unit hypercube  $G := \left\{ \frac{0}{h_1}, \dots, \frac{h_1}{h_1} \right\} \times \dots \times \left\{ \frac{0}{h_p}, \dots, \frac{h_p}{h_p} \right\}, \mathbf{h} = (h_1, \dots, h_p) \in \mathbb{N}^p$ , is written as follows:

$$B_{\mathbf{h}}(C)(\mathbf{u}) := \sum_{t_1=0}^{h_1} \dots \sum_{t_p=0}^{h_p} C\left(\frac{t_1}{h_1}, \dots, \frac{t_p}{h_p}\right) \prod_{j=1}^p P_{h_j, t_j}(u_j), \quad (4.2)$$

with  $\mathbf{u} = (u_1, \dots, u_p) \in [0, 1]^p$ , and the Bernstein polynomial  $P_{h,t}(u) := \frac{t!}{h!(t-h)!} u^h (1-u)^{t-h}$ . When  $C$  is a copula, then  $B_{\mathbf{m}}(C)$  is called “Bernstein copula”. Therefore, the empirical Bernstein copula is an application of the Bernstein polynomial in Eq. (4.2) to the so-called

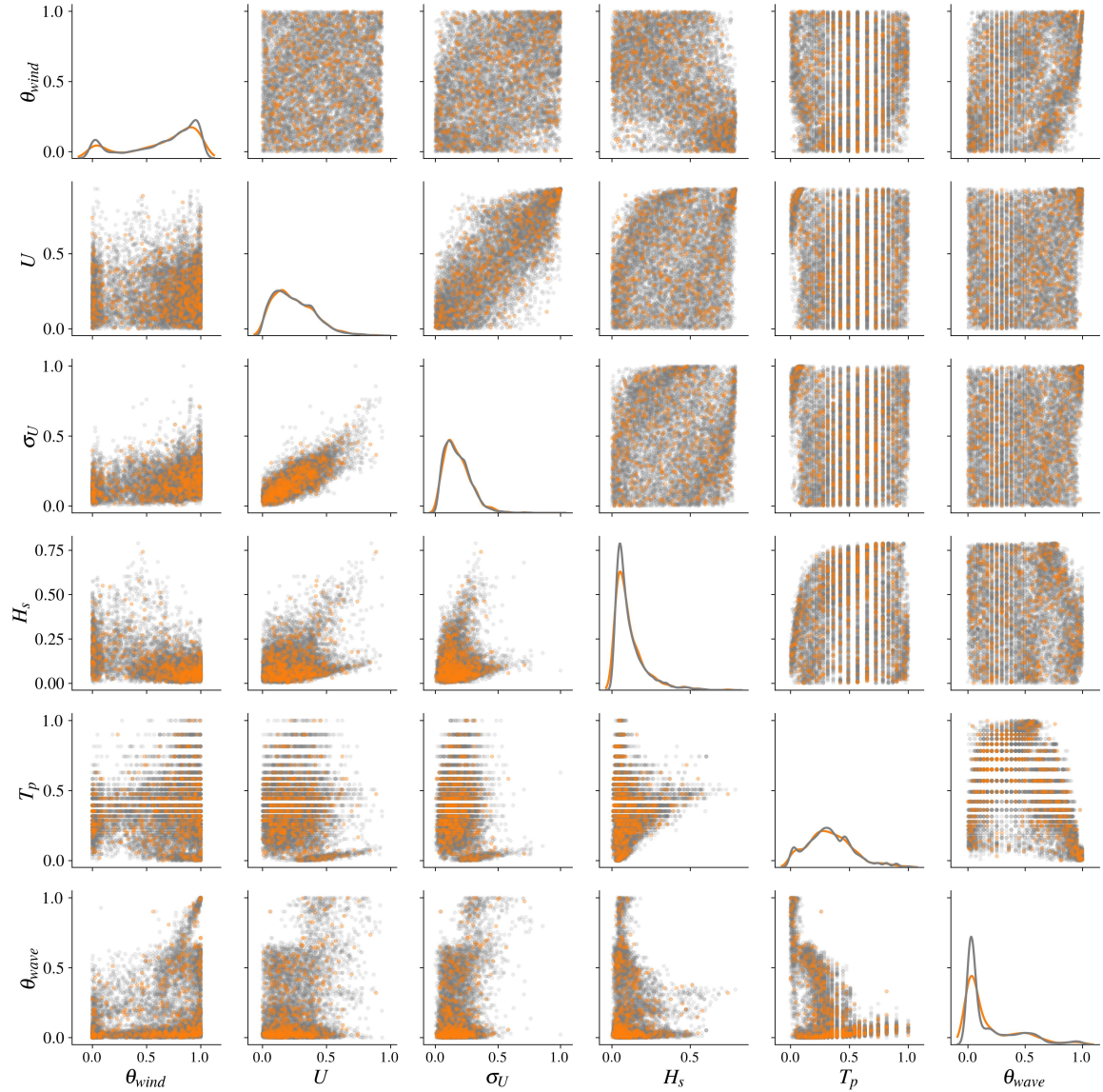


Fig. 4.4 Copulogram of the Teesside measured data ( $N = 10^4$  in grey), kernel herding subsample ( $n = 500$  in orange). Marginals are represented by univariate kernel density estimation plots (diagonal), the dependence structure with scatter plots in the ranked space (upper triangle). Scatter plots on the bottom triangle are set in the physical space

“empirical copula”. In practice, considering a sample  $\mathbf{X}_n = \{\mathbf{x}^{(1)}, \dots, \mathbf{x}^{(n)}\} \in \mathbb{R}^{np}$  and the associated ranked sample  $\mathbf{R}_n = \{\mathbf{r}^{(1)}, \dots, \mathbf{r}^{(n)}\}$ , the corresponding empirical copula is written:

$$C_n(\mathbf{u}) := \frac{1}{n} \sum_{i=0}^n \prod_{j=1}^p \mathbb{1} \left\{ \frac{r_j^{(i)}}{n} \leq u_j \right\}, \mathbf{u} = (u_1, \dots, u_p) \in [0, 1]^p. \quad (4.3)$$

Provided a large enough learning set  $\mathbf{X}_n$ , the EBC combined with kernel density estimation for the marginals fit well the environmental joint distribution related to the dataset in

Fig. 4.4. Moreover, the densities of the EBC are available in an explicit form, making Monte Carlo or quasi-Monte Carlo generation easy. For a thorough presentation of this method and theoretical results regarding the EBC tuning, see the manuscript of [44]. Further discussions and numerical experiments on the estimation of nonparametric copula models are presented in [58].

#### 4.2.4 Fatigue assessment

As described in Fig. 4.2, a typical DIEGO simulation returns a 10-minute multiaxial stress time series at each node  $i \in \mathbb{N}$  of the 1D meshed structure. Since fatigue laws are established for uniaxial stresses, the first step is to compute one equivalent Von Mises stress time series at each structural node.

However, the foundation and the tower of an OWT are a succession of tubes with various sections connected by bolted or welded joints. Our work studies the welded joints at the mudline level, identified as a critical area for the structure. To compute fatigue in this joint, the external circle of the welding ring is discretized for a few azimuth angles  $\theta \in \mathbb{R}_+$  (see the red points in the monopile cross-section on the right in Fig. 4.5). The equivalent Von Mises stress time series is then reported on the external welding ring for an azimuth  $\theta$ . According to [48] and our own experience, the most critical azimuth angles are roughly aligned with the main wind and wave directions (whose distributions are illustrated in Fig. 4.5). According to these illustrations, the wind and wave conditions have a very dominant orientation, which is explained by the closeness of the wind farm to the shore. Then, it is assumed that azimuth angles in these directions will be more solicited, leading to higher fatigue damage. To assess fatigue damage, rainflow counting [19] first identifies the stress cycles and their respective amplitudes (using the implementation of the ASTM E1049-85 rainflow cycle counting algorithm from the Python package `rainflow`<sup>2</sup>). For each identified stress cycle of amplitude  $s$ , the so-called “Stress vs. Number of cycles” curve (also called the “Wöhler curve”) allows one to estimate the number  $N_c$  of similar stress cycles necessary to reach fatigue ruin:

$$N_c := W(s) = as^{-m}, a \in \mathbb{R}, m \in \mathbb{R}. \quad (4.4)$$

Finally, a usual approach to compute the damage is to consider the fatigue contribution of each stress cycle identified using Miner’s rule. Damage occurring during a 10-minute operating time is simulated and then scaled up to the OWT lifetime. More details regarding damage assessment are available in Appendix ???. For a realization of environmental conditions  $\mathbf{x} \in \mathcal{D}_{\mathbf{X}}$ , at a structural node  $i$ , an azimuth angle  $\theta$ ;  $k$  stress cycles of respective amplitude  $\{s_{i,\theta}^{(j)}(\mathbf{x})\}_{j=1}^k$  are identified. Then, Miner’s rule [20] defines the damage function

---

<sup>2</sup><https://github.com/iamlikeme/rainflow>

$g_{i,\theta}(\mathbf{x}) : \mathcal{D}_{\mathbf{X}} \rightarrow \mathbb{R}_+$  by:

$$g_{i,\theta}(\mathbf{x}) = \sum_{j=1}^k \frac{1}{N_c^{(j)}} = \sum_{j=1}^k \frac{1}{W(s_{i,\theta}^{(j)}(\mathbf{x}))}. \quad (4.5)$$

As defined by the DNV standards for OWT fatigue design [17], the quantity of interest in the present paper is the “mean global damage”  $d_{i,\theta}$ , computed at the node  $i$ , for an azimuth angle  $\theta$ :

$$d_{i,\theta} = \mathbb{E}[g_{i,\theta}(\mathbf{X})] = \int_{\mathcal{D}_{\mathbf{X}}} g_{i,\theta}(\mathbf{x}) f_{\mathbf{X}}(\mathbf{x}) d\mathbf{x}. \quad (4.6)$$

To get a preview of the distribution of this output random variable  $g_{i,\theta}(\mathbf{X})$ , a histogram of a large Monte Carlo simulation ( $N_{\text{ref}} = 2000$ ) is represented in Fig. 4.6 (with a log scale). The log-damage presents a little asymmetry, so it is unlikely to be normally distributed.

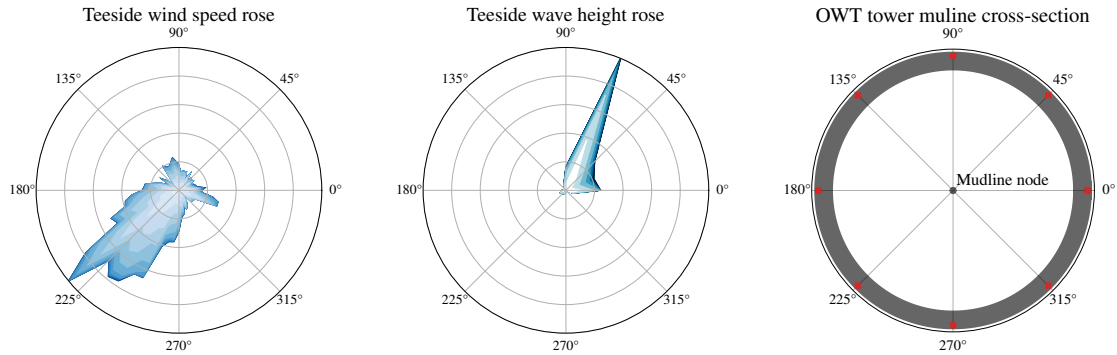


Fig. 4.5 Angular distribution of the wind and waves with a horizontal cross-section of the OWT structure and the mudline

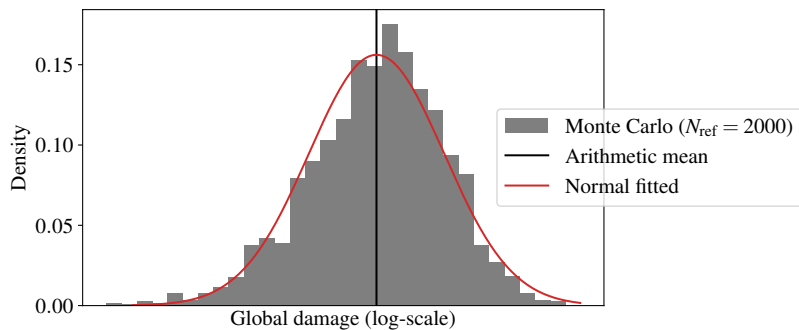


Fig. 4.6 Histogram of the log-damage, at mudline, azimuth 45 deg. (Monte Carlo reference sample)

## 4.3 Numerical integration procedures for mean damage estimation

### 4.3.1 Quadrature rules and quasi-Monte Carlo methods

The present section explores different methods aiming at estimating the expected value of a function against a probability measure. Considering a measurable space  $\mathcal{D}_X \subset \mathbb{R}^p$ ,  $p \in \mathbb{N}_+$ , associated with a known Lebesgue measure  $\mu$ , let us study the approximation of integrals of the form  $\int_{\mathcal{D}_X} g(\mathbf{x}) d\mu(\mathbf{x})$ , with  $g$  the map  $g(\mathbf{x}) : \mathcal{D}_X \rightarrow \mathbb{R}$ . This problem is equivalent to the central tendency estimation of  $\mathbf{Y} = g(\mathbf{X})$ , the image of the environmental random variable  $\mathbf{X}$  by the damage function  $g$  (see Eq. (4.6)). Some authors also named this generic problem *probabilistic integration* [6]. In practice, this quantity of interest is estimated on an  $n$ -sized set of damage realizations  $\mathbf{y}_n = \{g(\mathbf{x}^{(1)}), \dots, g(\mathbf{x}^{(n)})\}$  of an input sample  $\mathbf{X}_n = \{\mathbf{x}^{(1)}, \dots, \mathbf{x}^{(n)}\}$ . Our numerical experiment framework often implies that the function  $g$  is costly to evaluate, making the realization number limited. A weighted arithmetic mean of the realizations  $\{g(\mathbf{x}^{(1)}), \dots, g(\mathbf{x}^{(n)})\}$  is called a *quadrature rule* with a set of unconstrained weights  $\mathbf{w}_n = \{w_1, \dots, w_n\} \in \mathbb{R}^n$ :

$$I_\mu(g) := \int_{\mathcal{D}_X} g(\mathbf{x}) d\mu(\mathbf{x}) \approx \sum_{i=1}^n w_i g(\mathbf{x}^{(i)}). \quad (4.7)$$

For a given sample size  $n$ , our goal is to find a set of tuples  $\{\mathbf{x}^{(i)}, w_i\}_{i=1}^n$  (i.e., quadrature rule), giving the best approximation of our quantity. In the literature, a large panel of numerical integration methods has been proposed to tackle this problem. In a recent work, [76] applies a first family of numerical integration methods based on tensor products of quadrature rules to a similar industrial OWT use case. Unfortunately, the tensor formulation fails when inputs present a strong dependency structure and will not be studied in this paper. Alternatively, sampling methods rely on generating a set of points  $\mathbf{X}_n$  drawn from the input distribution to compute the arithmetic mean of their realizations (i.e., uniform weights  $\{w_i = \frac{1}{n}\}_{i=1}^n$ ). Among them, low-discrepancy sequences, also called “quasi-Monte Carlo” sampling (e.g., Sobol’, Halton, Faure sequences) are known to improve the standard Monte Carlo convergence rate and will be used as a deterministic reference method in the following numerical experiments [54].

### 4.3.2 Kernel discrepancy

**Quantization of probability measures and quadrature** When dealing with probabilistic integration such as Eq. (4.7), a quadrature rule is a finite representation of a continuous measure  $\mu$  by a discrete measure  $\zeta_n = \sum_{i=1}^n w_i \delta(\mathbf{x}^{(i)})$  (weighted sum of Dirac distributions at the design points  $\mathbf{X}_n$ ). In the literature, this procedure is also called *quantization* of a

continuous measure  $\mu$ . Overall, numerical integration is a particular case of probabilistic integration against a uniform input measure. For uniform measures, the Koksma-Hlawka inequality [54] provides a useful upper bound on the absolute error of a quadrature rule:

$$\left| \int_{[0,1]^p} g(\mathbf{x}) d\mathbf{x} - \frac{1}{n} \sum_{i=1}^n g(\mathbf{x}^{(i)}) \right| \leq V(g) D_n^*(\mathbf{X}_n). \quad (4.8)$$

As explained in [59],  $V(g) = \sum_{u \subseteq \{1, \dots, p\}} \int_{[0,1]^u} \left| \frac{\partial^u g}{\partial \mathbf{x}_u}(\mathbf{x}_u, 1) \right| d\mathbf{x}$ , quantifies the complexity of the integrand, while  $D_n^*(\mathbf{X}_n)$  evaluates the discrepancy to uniformity of the design  $\mathbf{X}_n$ . Therefore, the Koksma-Hlawka inequality shows that the quadrature rule's accuracy relies on the good quantization of  $\mu$  by  $\mathbf{X}_n$ . For a uniform target measure  $\mu$ , the star discrepancy is a metric assessing how far from uniformity a sample  $\mathbf{X}_n$  is. When generalizing to a non-uniform measure, a good quantization of  $\mu$  should also lead to a good approximation of the quantity.

**Reproducing kernel Hilbert space and kernel mean embedding** To generalize the Koksma-Hlawka inequality to any probability measure, let us assume that the integrand  $g$  lives in a specific function space  $\mathcal{H}(k)$ .  $\mathcal{H}(k)$  is a *reproducing kernel Hilbert space* (RKHS), which is an inner product space  $\mathcal{H}(k)$  of functions  $g : \mathcal{D}_{\mathbf{X}} \rightarrow \mathbb{R}$ . Considering a symmetric and positive definite function  $k : \mathcal{D}_{\mathbf{X}} \times \mathcal{D}_{\mathbf{X}} \rightarrow \mathbb{R}$ , later called a “reproducing kernel” or simply a “kernel”, an RKHS verifies the following axioms:

- The “feature map”  $\phi : \mathcal{D}_{\mathbf{X}} \rightarrow \mathcal{H}(k); \phi(\mathbf{x}) = k(\cdot, \mathbf{x})$  belongs to the RKHS:  $k(\cdot, \mathbf{x}) \in \mathcal{H}(k), \forall \mathbf{x} \in \mathcal{D}_{\mathbf{X}}$ .
- The “reproducing property”:  $\langle g, k(\cdot, \mathbf{x}) \rangle_{\mathcal{H}(k)} = g(\mathbf{x}), \quad \forall \mathbf{x} \in \mathcal{D}_{\mathbf{X}}, \forall g \in \mathcal{H}(k)$ .

Note that it can be shown that every positive semi-definite kernel defines a unique RKHS (and vice versa) with a feature map  $\phi$ , such that  $k(\mathbf{x}, \mathbf{x}') = \langle \phi(\mathbf{x}), \phi(\mathbf{x}') \rangle_{\mathcal{H}(k)}$ . This framework allows us to embed a continuous or discrete probability measure in an RKHS, as illustrated in Fig. 4.7. For any measure  $\mu$ , its *kernel mean embedding* [70], also called “potential”  $P_\mu(\mathbf{x})$  in [65], associated with the kernel  $k$  is defined as:

$$P_\mu(\mathbf{x}) := \int_{\mathcal{D}_{\mathbf{X}}} k(\mathbf{x}, \mathbf{x}') d\mu(\mathbf{x}'). \quad (4.9)$$

Respectively, the potential  $P_{\zeta_n}(\mathbf{x})$  of a discrete distribution  $\zeta_n = \sum_{i=1}^n w_i \delta(\mathbf{x}^{(i)})$ ,  $w_i \in \mathbb{R}$  associated with the kernel  $k$  can be written as:

$$P_{\zeta_n}(\mathbf{x}) = \int_{\mathcal{D}_{\mathbf{X}}} k(\mathbf{x}, \mathbf{x}') d\zeta_n(\mathbf{x}') = \sum_{i=1}^n w_i k(\mathbf{x}, \mathbf{x}^{(i)}). \quad (4.10)$$

The potential  $P_\mu(\mathbf{x})$  of the targeted measure  $\mu$  will be referred to as “target potential” and the potential  $P_{\zeta_n}(\mathbf{x})$  associated with the discrete distribution  $\zeta_n$  called “current potential”

when its support is the design  $\mathbf{X}_n$ . If  $P_{\zeta_n}(\mathbf{x})$  is close to  $P_\mu(\mathbf{x})$ , it can be interpreted to mean that  $\zeta_n$  is an adequate quantization or representation of  $\mu$  by the discrete distribution  $\zeta_n$  (and therefore lead to a good estimation of a quantity such as  $I_\mu(g)$  from Eq. (4.7)). Potentials can be computed in closed forms for specific pairs of distribution and associated kernel. Summary tables of some of these cases are detailed in [7] (section 3.4), [65] (section 4), and extended in [22]. However, in most cases, the target potentials must be estimated on a large and representative sample, typically a large quasi-Monte Carlo sample of  $\mu$ .

**Definition 1** *The energy of a measure  $\mu$  is defined as the integral of the potential  $P_\mu$  against the measure, which leads to the following scalar quantity:*

$$\varepsilon_\mu := \int_{\mathcal{D}_{\mathbf{X}}} P_\mu(\mathbf{x}) d\mu(\mathbf{x}) = \iint_{\mathcal{D}_{\mathbf{X}}^2} k(\mathbf{x}, \mathbf{x}') d\mu(\mathbf{x}) d\mu(\mathbf{x}'). \quad (4.11)$$

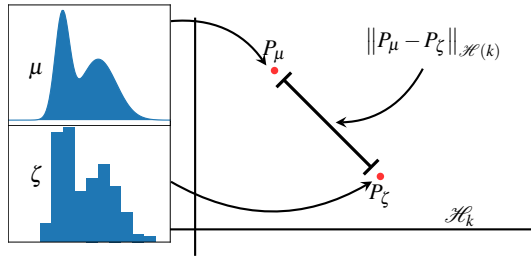


Fig. 4.7 Kernel mean embedding of a continuous and discrete probability distribution

Finally, using the reproducing property and writing the Cauchy-Schwarz inequality on the absolute quadrature error leads to the following inequality, similar to the Koksma-Hlawka inequality Eq. (4.8) (see [6]):

$$\left| \sum_{i=1}^n w_i g(\mathbf{x}^{(i)}) - \int_{\mathcal{D}_{\mathbf{X}}} g(\mathbf{x}) d\mu(\mathbf{x}) \right| = \left| \langle g, P_{\zeta_n}(\mathbf{x}) \rangle_{\mathcal{H}(k)} - \langle g, P_\mu(\mathbf{x}) \rangle_{\mathcal{H}(k)} \right| \quad (4.12a)$$

$$= \left| \langle g, (P_{\zeta_n}(\mathbf{x}) - P_\mu(\mathbf{x})) \rangle_{\mathcal{H}(k)} \right| \quad (4.12b)$$

$$\leq \|g\|_{\mathcal{H}(k)} \|P_\mu(\mathbf{x}) - P_{\zeta_n}(\mathbf{x})\|_{\mathcal{H}(k)}. \quad (4.12c)$$

**Maximum mean discrepancy** A metric of discrepancy and quadrature error is offered by the *maximum mean discrepancy* (MMD). This distance between two probability distributions  $\mu$  and  $\zeta$  is given by the worst-case error for any function within a unit ball of the Hilbert space  $\mathcal{H}(k)$ , associated with the kernel  $k$ :

$$\text{MMD}_k(\mu, \zeta) := \sup_{\|g\|_{\mathcal{H}(k)} \leq 1} \left| \int_{\mathcal{D}_{\mathbf{X}}} g(\mathbf{x}) d\mu(\mathbf{x}) - \int_{\mathcal{D}_{\mathbf{X}}} g(\mathbf{x}) d\zeta(\mathbf{x}) \right| \quad (4.13)$$

According to the inequality in Eq. (4.12c),  $\text{MMD}_k(\mu, \zeta) = \|P_\mu - P_\zeta\|_{\mathcal{H}(k)}$ , meaning that the MMD fully relies on the difference of potentials. Moreover, [72] defines a kernel as “characteristic kernel” when the following equivalence is true:  $\text{MMD}_k(\mu, \zeta) = 0 \Leftrightarrow \mu = \zeta$ . This property makes the MMD a metric on  $\mathcal{D}_{\mathbf{X}}$ . The squared MMD has been used for other purposes than numerical integration: e.g., statistical testing [25], and global sensitivity analysis [13]. It can be written as follows:

$$\text{MMD}_k(\mu, \zeta)^2 = \|P_\mu(\mathbf{x}) - P_\zeta(\mathbf{x})\|_{\mathcal{H}(k)}^2 \quad (4.14a)$$

$$= \langle (P_\mu(\mathbf{x}) - P_\zeta(\mathbf{x})), (P_\mu(\mathbf{x}) - P_\zeta(\mathbf{x})) \rangle_{\mathcal{H}(k)} \quad (4.14b)$$

$$= \langle P_\mu(\mathbf{x}), P_\mu(\mathbf{x}) \rangle_{\mathcal{H}(k)} - 2 \langle P_\mu(\mathbf{x}), P_\zeta(\mathbf{x}) \rangle_{\mathcal{H}(k)} + \langle P_\zeta(\mathbf{x}), P_\zeta(\mathbf{x}) \rangle_{\mathcal{H}(k)} \quad (4.14c)$$

$$= \iint_{\mathcal{D}_{\mathbf{X}}^2} k(\mathbf{x}, \mathbf{x}') d\mu(\mathbf{x}) d\mu(\mathbf{x}') - 2 \iint_{\mathcal{D}_{\mathbf{X}}^2} k(\mathbf{x}, \mathbf{x}') d\mu(\mathbf{x}) d\zeta(\mathbf{x}') + \iint_{\mathcal{D}_{\mathbf{X}}^2} k(\mathbf{x}, \mathbf{x}') d\zeta(\mathbf{x}) d\zeta(\mathbf{x}'). \quad (4.14d)$$

Taking a discrete distribution with uniform weights  $\zeta_n = \frac{1}{n} \sum_{i=1}^n \delta(\mathbf{x}^{(i)})$ , the squared MMD reduces to:

$$\text{MMD}_k(\mu, \zeta_n)^2 = \varepsilon_\mu - \frac{2}{n} \sum_{i=1}^n P_\mu(\mathbf{x}^{(i)}) + \frac{1}{n^2} \sum_{i,j=1}^n k(\mathbf{x}^{(i)}, \mathbf{x}^{(j)}). \quad (4.15)$$

### 4.3.3 Kernel herding sampling

Herein, the MMD is used to quantize the known target measure  $\mu$  by a design sample  $\mathbf{X}_n$ . For practical reasons, design construction is done sequentially. Sequential strategies can also be used to learn and validate regression models for statistical learning (see [22]). Moreover, since each realization is supposed to be obtained at the same unitary cost, we fix the quadrature weights as uniform during the construction of the design  $\mathbf{X}_n$ .

*Kernel herding* (KH), proposed by [12], is a sampling method that offers a quantization of the measure  $\mu$  by minimizing a squared MMD when adding points iteratively. With a current design  $\mathbf{X}_n$  and its corresponding discrete distribution with uniform weights  $\zeta_n = \frac{1}{n} \sum_{i=1}^n \delta(\mathbf{x}^{(i)})$ , a KH iteration can be written as an optimization problem involving the following criterion over the point  $\mathbf{x}^{(n+1)} \in \mathcal{D}_{\mathbf{X}}$ :

$$\mathbf{x}^{(n+1)} \in \arg \min_{\mathbf{x} \in \mathcal{D}_{\mathbf{X}}} \left\{ \text{MMD}_k \left( \mu, \frac{1}{n+1} \left( \delta(\mathbf{x}) + \sum_{i=1}^n \delta(\mathbf{x}^{(i)}) \right) \right)^2 \right\}. \quad (4.16)$$

In the literature, two formulations of this optimization problem can be found. The first one uses the Frank-Wolfe algorithm (or “conditional gradient algorithm”) to compute a

linearization of the problem under the convexity hypothesis (see [43] and [8] for more details). The second one is a straightforward greedy optimization. Due to the combinatorial complexity, the greedy formulation is tractable for sequential construction. To see this, let us develop the MMD from Eq. (4.15):

$$\text{MMD}_k \left( \mu, \frac{1}{n+1} \left( \delta(\mathbf{x}) + \sum_{i=1}^n \delta(\mathbf{x}^{(i)}) \right) \right)^2 = \varepsilon_\mu - \frac{2}{n+1} \sum_{i=1}^{n+1} P_\mu(\mathbf{x}^{(i)}) + \frac{1}{(n+1)^2} \sum_{i,j=1}^{n+1} k(\mathbf{x}^{(i)}, \mathbf{x}^{(j)}) \quad (4.17a)$$

$$= \varepsilon_\mu - \frac{2}{n+1} \left( P_\mu(\mathbf{x}) + \sum_{i=1}^n P_\mu(\mathbf{x}^{(i)}) \right) \quad (4.17b)$$

$$+ \frac{1}{(n+1)^2} \left( \sum_{i,j=1}^n k(\mathbf{x}^{(i)}, \mathbf{x}^{(j)}) + 2 \sum_{i=1}^n k(\mathbf{x}^{(i)}, \mathbf{x}) - k(\mathbf{x}, \mathbf{x}) \right). \quad (4.17c)$$

In the previously developed expression, only a few terms actually depend on the next optimal point  $\mathbf{x}^{(n+1)}$  since the target energy, denoted by  $\varepsilon_\mu$ , and  $k(\mathbf{x}, \mathbf{x}) = \sigma^2$  are constant (by taking a stationary kernel). Therefore, the greedy minimization of the MMD can be equivalently written as:

$$\mathbf{x}^{(n+1)} \in \arg \min_{\mathbf{x} \in \mathcal{D}_{\mathbf{X}}} \left\{ \frac{1}{n+1} \sum_{i=1}^n k(\mathbf{x}^{(i)}, \mathbf{x}) - P_\mu(\mathbf{x}) \right\} = \arg \min_{\mathbf{x} \in \mathcal{D}_{\mathbf{X}}} \left\{ \frac{n}{n+1} P_{\zeta_n}(\mathbf{x}) - P_\mu(\mathbf{x}) \right\}. \quad (4.18)$$

**Remark 1** For the sequential and uniformly weighted case, the formulation in Eq. (4.18) is almost similar to the Frank-Wolfe formulation. Our numerical experiments showed that these two versions generate very close designs, especially as  $n$  becomes large. [64] express the Frank-Wolfe formulation in the sequential and uniformly weighted case as follows:

$$\mathbf{x}^{(n+1)} \in \arg \min_{\mathbf{x} \in \mathcal{D}_{\mathbf{X}}} \left\{ P_{\zeta_n}(\mathbf{x}) - P_\mu(\mathbf{x}) \right\}. \quad (4.19)$$

**Remark 2** In practice, the optimization problem is solved by a brute-force approach on a fairly dense finite subset  $\mathcal{S} \subseteq \mathcal{D}_{\mathbf{X}}$  of candidate points with size  $N \gg n$  that emulates the target distribution, also called the “candidate set”. This sample is also used to estimate the target potential  $P_\mu(\mathbf{x}) \approx \frac{1}{N} \sum_{i=1}^N k(\mathbf{x}^{(i)}, \mathbf{x})$ .

As explained previously, choosing the kernel defines the function space on which the worst-case function is found (see Eq. (4.13)). Therefore, this sampling method is sensitive to kernel choice. A kernel is defined, both by the choice of its parametric family (e.g., Matérn, squared exponential) and the choice of its tuning. The so-called “support points”

method developed by [49] is a special case of kernel herding that uses the characteristic and parameter-free ‘‘energy-distance’’ kernel (introduced by [74]). In the following numerical experiments, the energy-distance kernel will be compared with an isotropic tensor product of a Matérn kernel (with regularity parameter  $v = 5/2$  and correlation lengths  $\theta_i$ ), or a squared exponential kernel (with correlation lengths  $\theta_i$ ) defined in Table 4.3. Since the Matérn and squared exponential kernels are widely used for Gaussian process regression [66], they were naturally picked to challenge the energy-distance kernel. The correlation lengths for the squared exponential and Matérn kernels are set using the heuristic given in [22],  $\theta_i = n^{-1/p}, i \in \{1, \dots, p\}$ .

Table 4.3 Kernels considered in the following numerical experiments.

Energy-distance	$k_E(\mathbf{x}, \mathbf{x}') = \frac{1}{2} (\ \mathbf{x}\  + \ \mathbf{x}'\  - \ \mathbf{x} - \mathbf{x}'\ )$	
Squared exponential	$k_G(\mathbf{x}, \mathbf{x}') = \prod_{i=1}^p k_{\theta_i}(x_i - x'_i)$	$k_{\theta}(x - x') = \exp\left(-\frac{(x-x')^2}{2\theta^2}\right)$
Matérn ( $v = 5/2$ )	$k_M(\mathbf{x}, \mathbf{x}') = \prod_{i=1}^p k_{5/2, \theta_i}(x_i - x'_i)$	$k_{5/2, \theta}(x - x') = \left(1 + \frac{\sqrt{5}}{\theta} x - x' \right) \exp\left(-\frac{\sqrt{5}}{\theta} x - x' \right)$

Fig. 4.8 represents the covariance structure of the three kernels. One can notice that the squared exponential and Matérn  $v = 5/2$  kernels are closer to one another than they are to the energy-distance. In fact, as  $v$  tends to infinity, the Matérn kernel tends toward the squared exponential kernel (which has infinitely differentiable sample paths, see [66]). For these two stationary kernels, the correlation length controls how fast the correlation between two points decreases as their distance from one another increases. Meanwhile, the energy distance is not stationary (but still positive and semi-definite). Therefore, its value does not only depend on the distance between two points but also on the norm of each of the points.

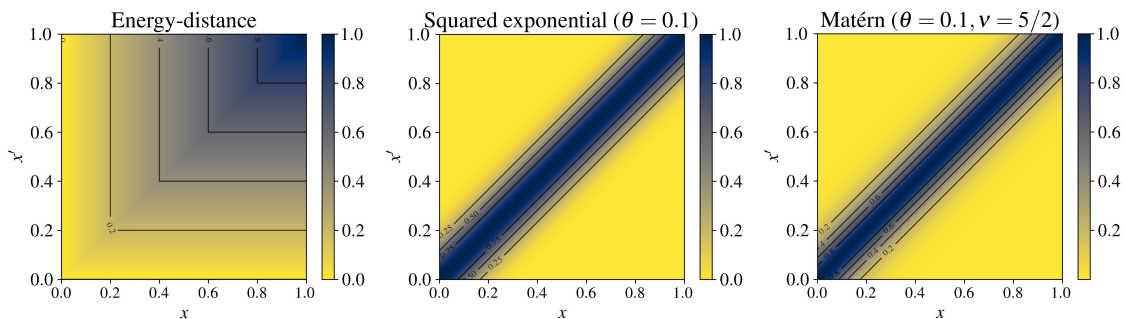


Fig. 4.8 Kernel illustrations (left to right: energy-distance, squared exponential, and Matérn 5/2)

To illustrate the sequential sampling of a complex distribution, Fig. 4.9 shows three nested kernel herding samples (orange crosses for different sizes  $n \in \{10, 20, 40\}$ ) of a mixture of Gaussian distributions with complex nonlinear dependencies (with density represented by the black isoprobability contours). In this example, the method seems to build a parsimonious design between each mode of the distribution. The candidate set (in light grey) was generated by a large quasi-Monte sample of the underlying Gaussian mixture. In this two-dimensional case, this candidate set is sufficient to estimate the target potential  $P_\mu$ . However, the main bottleneck of kernel herding is the estimation of the potentials, which becomes costly in high dimension.

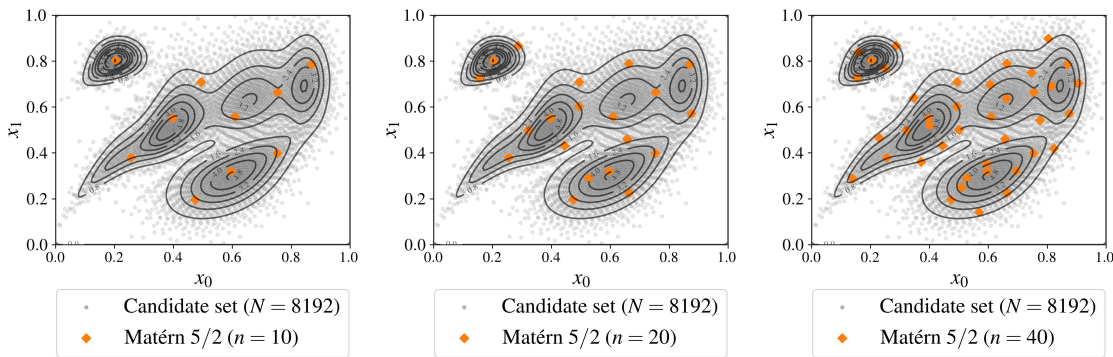


Fig. 4.9 Sequential kernel herding for increasing design sizes ( $n \in \{10, 20, 40\}$ ) built on a candidate set of  $N = 8192$  points drawn from a complex Gaussian mixture  $\mu$

Other approaches take advantage of the progressive knowledge acquired sequentially on  $g$  to select the following points in the design. These methods are sometimes called “active learning” or “adaptive strategies” [23]. Many of them rely on a sequentially updated Gaussian process (or Kriging) metamodel. To solve a probabilistic integration problem, the concept of Bayesian quadrature is introduced in the following.

#### 4.3.4 Bayesian quadrature

**Gaussian processes for Bayesian quadrature** Kernel methods and Gaussian processes present a lot of connections and equivalences, thoroughly reviewed by [36]. In numerical integration, Gaussian processes have been used to build quadrature rules in the seminal paper of [60], introducing the concept of *Bayesian quadrature* (BQ). Let us recall the probabilistic integration problem  $I_\mu(g) = \int_{\mathcal{D}_X} g(\mathbf{x}) d\mu(\mathbf{x})$  (introduced in Eq. (4.7)). From a general point of view, this quantity could be generalized by composing  $g$  with another function  $\psi$  (e.g., other moments, quantiles, exceedance probabilities). The quantity of interest then becomes,  $I_\mu(\psi(g))$ , for example when  $\psi$  is a monomial, it gives a moment the distribution of the output.

Let us assume, adopting a Bayesian point of view, that  $\xi$  is a stochastic process describing the uncertainty affecting the knowledge about the true function  $g$ . Let  $\xi$  be a Gaussian

process (GP) prior with a zero trend (denoted by  $\mathbf{0}$ ) to ease the calculation, and a stationary covariance kernel (denoted by  $k(\cdot, \cdot)$ ). The conditional posterior  $\xi_n := (\xi | \mathbf{y}_n) \sim \mathcal{GP}(\eta_n, s_n^2)$  has been conditioned on the function observations  $\mathbf{y}_n = [g(\mathbf{x}^{(1)}), \dots, g(\mathbf{x}^{(n)})]^\top$  computed from the input design  $\mathbf{X}_n$  and is fully defined by the well-known ‘‘Kriging equations’’ (see e.g., [66]):

$$\begin{cases} \eta_n(\mathbf{x}) := \mathbf{k}_n^\top(\mathbf{x}) \mathbf{K}_n^{-1} \mathbf{y}_n \\ s_n^2(\mathbf{x}) := k_n(\mathbf{x}, \mathbf{x}) - \mathbf{k}_n^\top(\mathbf{x}) \mathbf{K}_n^{-1} \mathbf{k}_n(\mathbf{x}) \end{cases} \quad (4.20)$$

where  $\mathbf{k}_n(\mathbf{x})$  is the column vector of the covariance kernel evaluations  $[k_n(\mathbf{x}, \mathbf{x}^{(1)}), \dots, k_n(\mathbf{x}, \mathbf{x}^{(n)})]$  and  $\mathbf{K}_n$  is the  $(n \times n)$  variance-covariance matrix such that the  $(i, j)$ -element is  $\{\mathbf{K}_n\}_{i,j} = k_n(\mathbf{x}^{(i)}, \mathbf{x}^{(j)})$ .

In BQ, the main object is the random variable  $I_\mu(\xi_n)$ . According to [6], its distribution on  $\mathbb{R}$  is the pushforward of  $\xi_n$  through the integration operator  $I_\mu(\cdot)$ , sometimes called *posterior distribution*:

$$I_\mu(\xi_n) = \int_{\mathcal{D}_X} (\xi(\mathbf{x}) | \mathbf{y}_n) d\mu(\mathbf{x}) = \int_{\mathcal{D}_X} \xi_n(\mathbf{x}) d\mu(\mathbf{x}). \quad (4.21)$$

Fig. 4.10 provides a one-dimensional illustration of the Bayesian quadrature of an unknown function (dashed black curve) against a given input measure  $\mu$  (with corresponding grey distribution at the bottom). For an arbitrary design, one can fit a Gaussian process model, interpolating the function observations (black crosses). Then, multiple trajectories of this conditioned Gaussian process  $\xi_n$  are drawn (orange curves) whilst its mean function, also called ‘‘predictor’’, is represented by the red curve. Therefore, the input measure  $\mu$  is propagated through the conditioned Gaussian process to obtain the random variable  $I_\mu(\xi_n)$ , with distribution represented on the right plot (brown curve). Again on the right plot, remark how the mean of this posterior distribution (brown line) is closer to the reference output expected value (dashed black line) than the arithmetic mean of the observations (black line). This plot was inspired by the paper of [29].

**Optimal weights computed by Bayesian quadrature** Taking the random process  $\xi_n$  as Gaussian conveniently implies that its posterior distribution  $a_\mu(\xi_n)$  is also Gaussian. This comes from the linearity of the infinite sum of realizations of a Gaussian process. The posterior distribution is described in a closed form through its mean and variance by applying Fubini’s theorem (see the supplementary materials from [6] for the proof regarding the variance):

$$\bar{y}_n^{\text{BQ}} := \mathbb{E}[I_\mu(\xi_n) | \mathbf{y}_n] = \int_{\mathcal{D}_X} \eta_n(\mathbf{x}) d\mu(\mathbf{x}) = \left[ \int_{\mathcal{D}_X} \mathbf{k}_n^\top(\mathbf{x}) d\mu(\mathbf{x}) \right] \mathbf{K}_n^{-1} \mathbf{y}_n = P_\mu(\mathbf{X}_n) \mathbf{K}_n^{-1} \mathbf{y}_n, \quad (4.22)$$

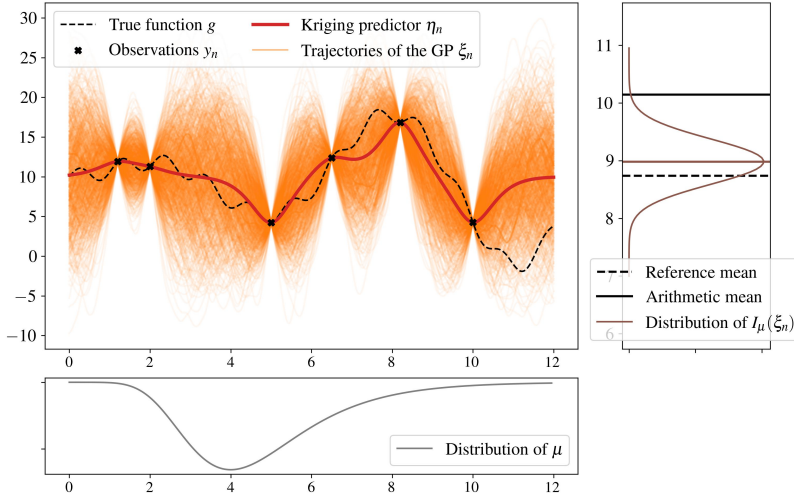


Fig. 4.10 Bayesian quadrature on a one-dimensional case

$$(\sigma_n^{\text{BQ}})^2 := \text{Var}(I_\mu(\xi_n)) = \iint_{\mathcal{D}_{\mathbf{X}^2}} k_n(\mathbf{x}, \mathbf{x}') d\mu(\mathbf{x}) d\mu(\mathbf{x}') = \varepsilon_\mu - P_\mu(\mathbf{X}_n) \mathbf{K}_n^{-1} P_\mu(\mathbf{X}_n)^\top. \quad (4.23)$$

Where  $P_\mu(\mathbf{X}_n)$  is the row vector of potentials  $\left[ \int k_n(\mathbf{x}, \mathbf{x}^{(1)}) d\mu(\mathbf{x}), \dots, \int k_n(\mathbf{x}, \mathbf{x}^{(n)}) d\mu(\mathbf{x}) \right]$ , and  $\varepsilon_\mu$  is given in Eq. (1). As in the one-dimensional example presented in Fig. 4.10, the expected value of  $I_\mu(\xi_n)$  expressed in Eq. (4.22) is a direct estimator of the quantity of interest Eq. (4.7). The so-called “Bayesian quadrature estimator” appears to be a simple linear combination of the observations by taking the row vector of “optimal weights” as:

$$\mathbf{w}_{\text{BQ}} := P_\mu(\mathbf{X}_n) \mathbf{K}_n^{-1} \quad (4.24)$$

For any given sample, an optimal set of weights can be computed, leading to the mean of the posterior distribution. Remark here that this enhancement depends on the evaluation of the inverse variance-covariance matrix  $\mathbf{K}_n^{-1}$ , which can present numerical difficulties, either when design points are too close, making the conditioning bad. Moreover, a prediction interval on the BQ estimator can be computed since the posterior distribution is Gaussian, with a variance expressed in closed-form in Eq. (4.23). The expressions in Eq. (4.22) and Eq. (4.23) were extended to Gaussian processes in the case of constant and linear trends in [65]. In the following numerical experiments, the expression with a hypothesis of constant trend  $\beta_n$  is used, which leads to:

$$\mathbb{E}[I_\mu(\xi_n)] = \beta_n + P_\mu(\mathbf{X}_n) \mathbf{K}_n^{-1} (\mathbf{y}_n - \beta_n \mathbf{1}_n). \quad (4.25)$$

Then, an a posteriori 95% prediction interval around the mean Bayesian estimator is directly given by:

$$\bar{y}_n^{\text{BQ}} \in [\bar{y}_n^{\text{BQ}} - 2\sigma_n^{\text{BQ}}, \bar{y}_n^{\text{BQ}} + 2\sigma_n^{\text{BQ}}]. \quad (4.26)$$

**Variance-based Bayesian quadrature rule** The link between the posterior variance and the squared MMD has been first made by [29] in their Proposition 1: the expected variance in the Bayesian quadrature  $\text{Var}(I_\mu(\xi_n))$  is the MMD between the target distribution  $\mu$  and  $\zeta_n = \sum_{i=1}^n \mathbf{w}_{\text{BQ}}^{(i)} \delta(\mathbf{x}^{(i)})$ . The proof is reproduced below (as well as in Proposition 6.1 from [36]):

$$\text{Var}(I_\mu(\xi_n)) = \mathbb{E} \left[ (I_\mu(\xi_n) - I_{\zeta_n}(\xi_n))^2 \right] \quad (4.27a)$$

$$= \mathbb{E} \left[ \left( \langle \xi_n, P_\mu \rangle_{\mathcal{H}(k)} - \langle \xi_n, P_{\zeta_n} \rangle_{\mathcal{H}(k)} \right)^2 \right] \quad (4.27b)$$

$$= \mathbb{E} \left[ \langle \xi_n, P_\mu - P_{\zeta_n} \rangle_{\mathcal{H}(k)}^2 \right] \quad (4.27c)$$

$$= \|P_\mu - P_{\zeta_n}\|_{\mathcal{H}(k)}^2 \quad (4.27d)$$

$$= \text{MMD}_k(\mu, \zeta_n)^2. \quad (4.27e)$$

Note that the transition from equation (27c) to (27d) relies on the property stating that if  $\xi$  is a standard Gaussian process then  $\forall g \in \mathcal{H}(k) : \langle \xi, g \rangle_{\mathcal{H}(k)} \sim \mathcal{N}(0, \|g\|_{\mathcal{H}(k)}^2)$ . The method that sequentially builds a quadrature rule by minimizing this variance is called by the authors “Sequential Bayesian Quadrature” (SBQ). According to the previous proof, this criterion can be seen as an optimally-weighted version of the kernel herding criterion, as stated in the title of the paper from [29]. Later, [8] proved the weak convergence of  $I_\mu(\xi_n)$  towards the target integral. Closer to wind turbines applications, [27] and [28] introduced the “Adaptive Kriging Damage Assessment” method: a Kriging-based method for mean damage estimation that is very close to SBQ. However, This type of method inherits the limits from both KH and BQ since it searches for optimal design points among a candidate set and computes an inverse variance-covariance matrix. These numerical operations both scale hardly in high dimension.

**Remark 3** *Every quadrature method introduced in this section has been built without any observation of the possibly costly function  $g$ . Therefore, they cannot be categorized as active learning approaches. Contrarily, [35] presents a set of methods for BQ with transformations (i.e., adding a positivity constraint on the function  $g$ ), which are truly active learning methods.*

## 4.4 Numerical experiments

This section presents numerical results computed on two different analytical toy-cases, respectively in dimension 2 (toy-case #1) and dimension 10 (toy-case #2), with easy-to-

evaluate functions  $g(\cdot)$  and associated input distributions  $\mu$ . Therefore, reference values can easily be computed with great precision. For each toy-case a large reference Monte Carlo sample ( $N_{\text{ref}} = 10^8$ ) is taken. This first benchmark compares the mean estimation of toy-cases given by quasi-Monte Carlo Sobol' sequences (abbreviation by QMC in the next figures), and kernel herdings with the three kernels defined in Table 4.3. Notice that the quasi-Monte Carlo designs are first generated on the unit cube, then transformed using the generalized Nataf transformation to follow the target distribution [47]. Additionally, the performances of kernel herding for both uniform and optimally-weighted Eq. (4.25) estimators are compared.

The kernel-based sampling and BQ methods were implemented in a new open-source Python package named `otkerneledesign`<sup>3</sup>. This development mostly relies on Open-TURNS<sup>4</sup>, an “Open source initiative for the Treatment of Uncertainties, Risks’N Statistics”, see [5]. The following numerical experiments are available in the Git repository named `ctbenchmark`<sup>5</sup>.

#### 4.4.1 Illustration through analytical toy-cases

The toy-cases were chosen to cover a large panel of complex probabilistic integration problems, completing the ones from [? ]. To assess the complexity of numerical integration problems, [61] introduced the concept of the “effective dimension” of an integrand function (number of the variables that actually impact the integral). The author showed that functions built on sums yield a low effective dimension (unlike functions built on products). In the same vein, [41] build three classes of integrand sorted by difficulty depending on their effective dimension:

- *class A*: problem with a few dominant variables.
- *class B*: problem without unimportant variables, and important low-order interaction terms.
- *class C*: problems without unimportant variables, and important high-order interaction terms.

The 10-dimensional “GSobol function” (toy-case #2) with a set of coefficient  $\{a_i = 2\}_{i=1}^{10}$  has an effective dimension equal to 10 and belongs to the hardest class C from [41]. In the case of the two-dimensional Gaussian mixture problem, the complexity is carried by the mixture of Gaussian distributions with highly nonlinear dependencies. Probabilistic integration results are presented in Fig. 4.11 (toy-case #1) and Fig. 4.12 (toy-case #2). Kernel herding samples with kernels defined in Table 4.3 (squared exponential in green, Matérn

---

<sup>3</sup><https://efekhari27.github.io/otkerneledesign/master/index.html>

<sup>4</sup><https://openturns.github.io/www/>

<sup>5</sup><https://github.com/efekhari27/ctbenchmark>

in orange, and energy-distance in red), are compared with a quasi-Monte Carlo sample (Sobol' sequences in grey). Convergences of the arithmetic means are plotted on the left and MMDs on the right. The respective BQ estimators of the means are plotted in dashed lines.

Table 4.4 Analytical toy-cases

<b>Toy-case #1</b>	$dim = 2$	$g_1(\mathbf{x}) = x_1 + x_2$	Gaussian mixture from Fig. 4.9
<b>Toy-case #2</b>	$dim = 10$	$g_2(\mathbf{x}) = \prod_{i=1}^{10} \frac{ 4x_i - 2  + a_i}{1 + a_i}, \{a_i = 2\}_{i=1}^{10}$	Gaussian $\mathcal{N}(\mathbf{0.5}, \mathbf{I}_{10})$

**Remark 4** *Different kernels are used in these numerical experiments. First, the generation kernel, used by the kernel herding algorithm to generate designs (with the heuristic tuning defined in Section 4.3.3). Second, the BQ kernel allows computation of the optimal weights (arbitrarily set up as a Matérn 5/2 with the heuristic tuning). Third, the evaluation kernel, which must be common to allow a fair comparison of the computed MMD results (same as the BQ kernel).*

*About toy-case #1.* KH consistently converges faster than quasi-Monte Carlo in this case, especially for small sizes in terms of MMD. BQ weights tend to reduce the fluctuations in the mean convergence, which ensures better performance for any size. Overall, applying the weights enhances the convergence rate.

*About toy-case #2.* Although quasi-Monte Carlo is known to suffer the “curse of dimensionality”, KH does not outperform it drastically in this example. In fact, KH with uniform weights performs worse than quasi-Monte Carlo while optimally-weighted KH does slightly better. Moreover, the results confirm that  $MMD_{BQ} < MMD_{unif}$  for all our experiments. The application of optimal-weights to the quasi-Monte Carlo sample slightly improves the estimation on this case. Note that the prediction interval around the BQ estimator is not plotted for the sake of readability.

In these two toy-cases, the MMD is shown to quantify numerical integration convergence well, which illustrates the validity of the inequality given in Eq. (4.12c), similar to the Koksma-Hlawka inequality, recalled in Eq. (4.8).

#### 4.4.2 Application to the Teesside wind turbine fatigue estimation

Before analyzing the performance of the KH on the industrial application, let us notice that the copulogram Fig. 4.14 seems to be in line with the global sensitivity analysis presented in [56] and [48]. In particular, the fact that the scatter plot of mean wind speed vs. turbulence wind speed is the main factor explaining the variance of the output  $Y = g(\mathbf{X})$ . Judging from these references, the numerical model does not seem to have high effective dimension,

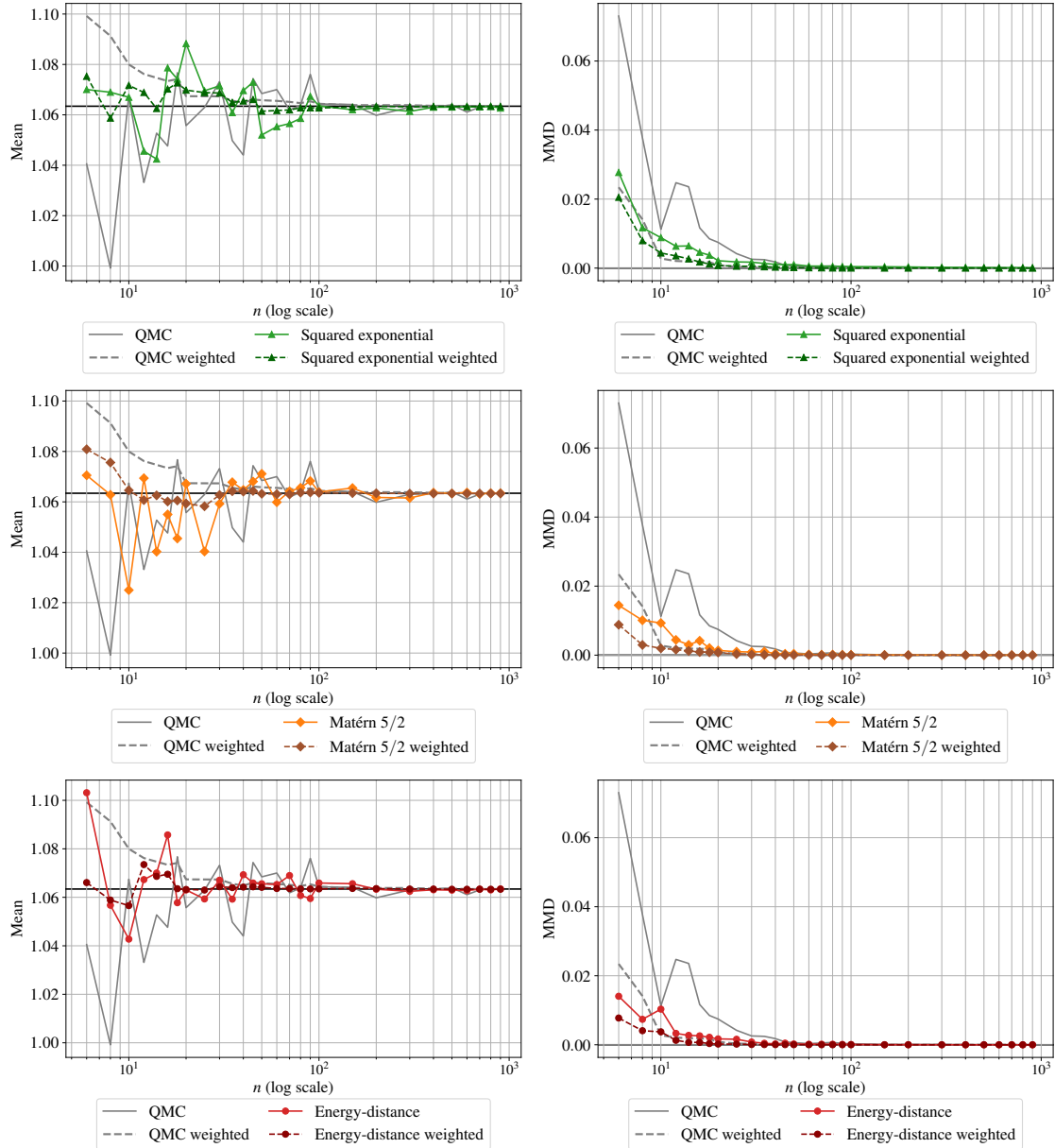


Fig. 4.11 Analytical benchmark results on the toy-case #1

however, the input dependence structure is challenging and the damage assessment induces strong nonlinearities (see Eq. (4.4)).

Crude Monte Carlo and kernel herding both subsample directly from a large dataset (previously referred to as candidate set). Unlike them, quasi-Monte Carlo generates a uniform sample in the unit hypercube, which can then be transformed according to a target distribution. In our case, this distribution is only known empirically via the candidate set. Since its dependence structure is complex (see Fig. 4.4), a parametric model might fit the distribution poorly (and therefore lead to a poor quasi-Monte Carlo estimation of the quantity). Then, a nonparametric fit using the empirical Bernstein copula (introduced in Section 4.2.3) coupled with a kernel density estimation on each marginal is applied to

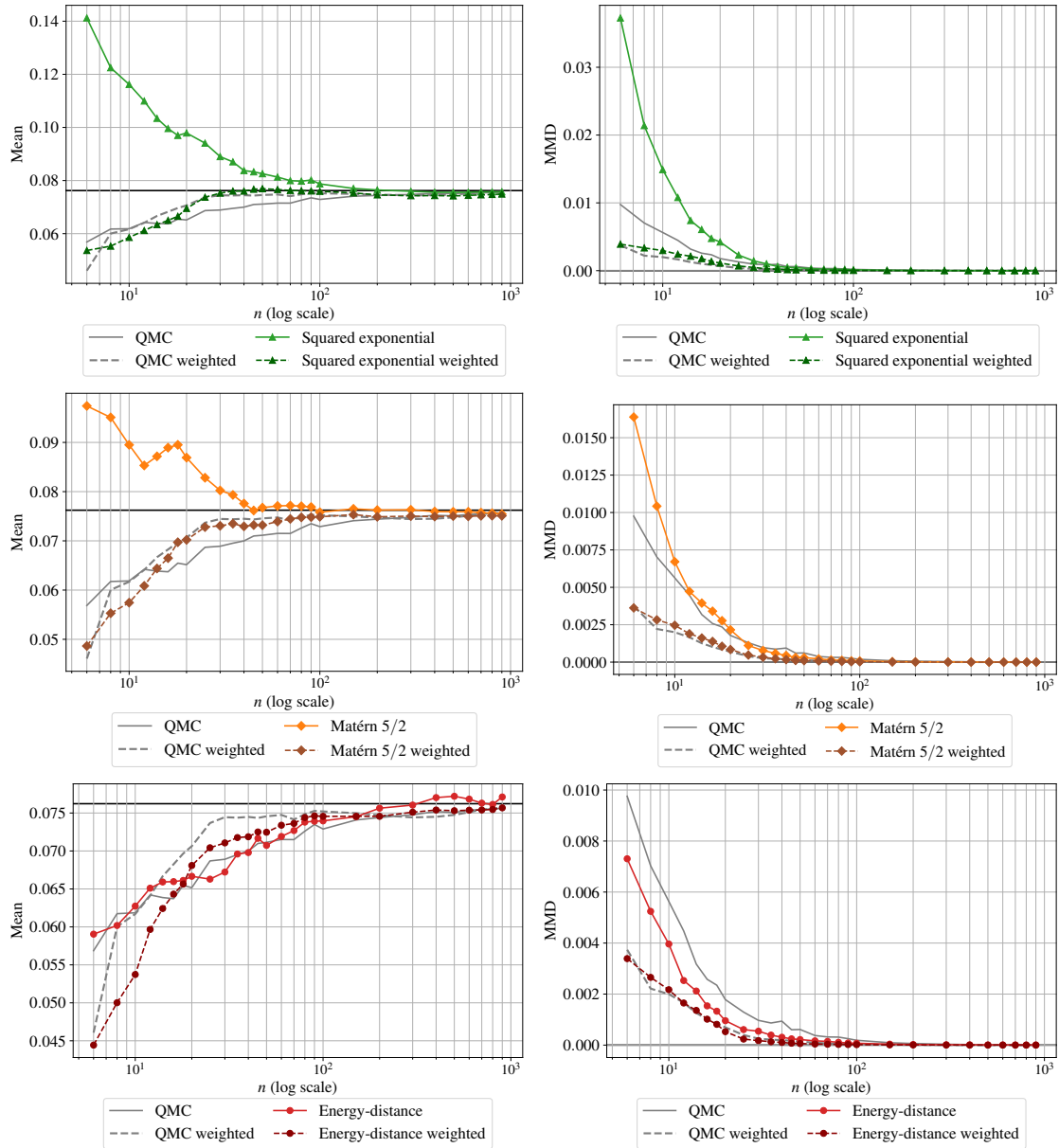


Fig. 4.12 Analytical benchmark results on the toy-case #2

the candidate set (with the EBC parameter  $m = 100 > m_{MISE}$  to avoid bias). Subsequently, quasi-Monte Carlo sampling is applied to this nonparametric model. These two approaches are summarized in Fig. 4.13, showing a practical advantage to the subsampling methods.

The results presented are compared in the following to a reference Monte Carlo sample with a confidence interval computed by bootstrap (see Fig. 4.15). The performance of the KH is good: it quickly converges towards the confidence interval of the Monte Carlo obtained with the reference sample. In addition, the Bayesian quadrature estimator also offers a posteriori prediction interval, which can reassure the user. The BQ prediction intervals are smaller than the ones obtained by bootstrap on the reference Monte Carlo sample. To provide more representative results, note that a set of scale parameters is computed with a

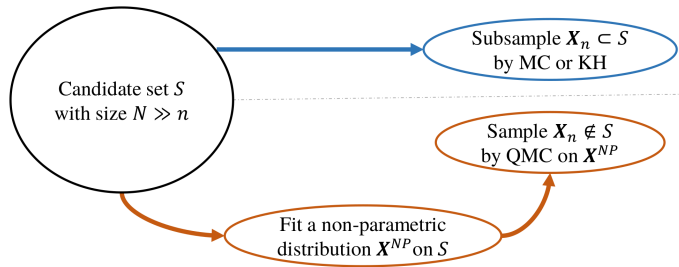


Fig. 4.13 Sampling techniques used for the industrial use case

kriging procedure to define the kernel used to compute BQ intervals. Since other methods do not generate independent samples, bootstrapping them is not legitimate. Contrarily to the other kernel, we observe that the energy-distance kernel presents a small bias with the MC reference for most of the azimuth angles computed in this experiment. Finally, combining nonparametric fitting with quasi-Monte Carlo sampling also delivers good results as long as the fitting step does not introduce a bias.

## 4.5 Conclusion

Wind energy assets are subject to highly uncertain environmental conditions. Uncertainty propagation through numerical models is performed to ensure their structural integrity (and energy production). For this case, the method recommended by the standards (regular grid sampling) is intractable. This can lead, in practice, to poor uncertainty propagation under the constraint of a simulation budget. This industrial use case induces two practical constraints. First, active learning methods are hard to set up on such a numerical model, and they restrict the use of high-performance computers. Second, the input distribution of the environmental conditions presents a complex dependence structure, hard to model with parametric approaches.

In this paper, the association of kernel herding sampling with Bayesian quadrature for central tendency has been both explored theoretically and numerically. This method fits with the practical constraints induced by the industrial use case. Kernel herding sampling subsamples the relevant points directly from a given dataset (here from the measured environmental data). Moreover, the method is fully compatible with intensive high-performance computer use. This work provides an MMD-based upper bound on numerical integration absolute error. Kernel herding and Bayesian quadrature both aim at finding the quadrature rule minimizing the MMD, and therefore the absolute integration error. The numerical experiments confirmed that the MMD is an appropriate criterion since it leads to results being better or equivalent to quasi-Monte Carlo sampling. This numerical benchmark relied on the Python package, called `otkerneledesign`, implementing the methods.

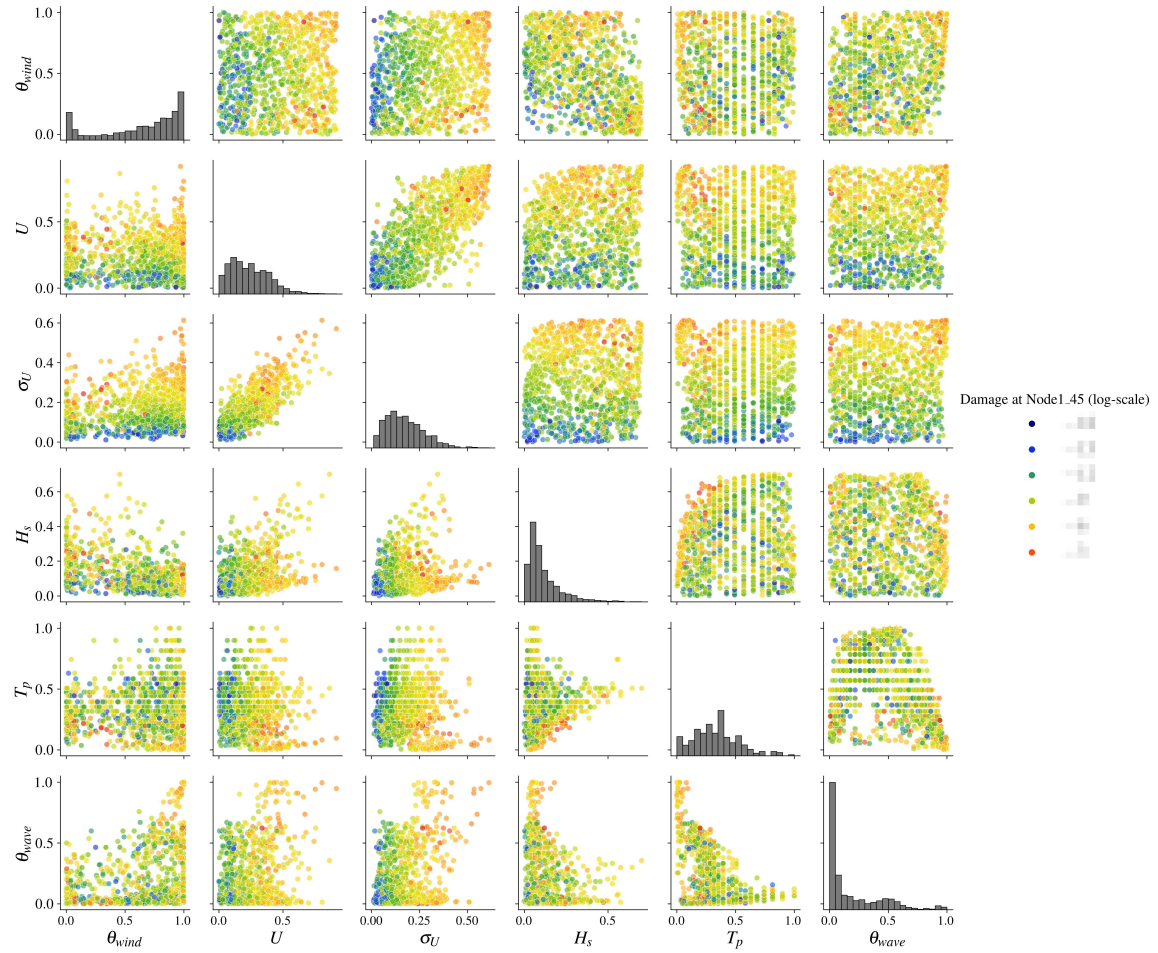


Fig. 4.14 Copulogram of the kernel herding design of experiments with corresponding outputs in color (log-scale) on the Teesside case ( $n = 10^3$ ). The highest values are in red while the lowest values are in blue. Marginals are represented by histograms (diagonal), the dependence structure with scatter plots in the ranked space (upper triangle). Scatter plots on the bottom triangle are set in the physical space.

The limits of this method are reached when the problem dimension increases considerably. Moreover, it showed to be sensitive to the choice of the kernel and its tuning (although good practices were offered). From a methodological point of view, further interpretation of the impact of the different kernels should be explored. Then, the kernel herding sampling could be used to estimate quantiles, following the work on randomized quasi-Monte Carlo for quantiles of [37]. Kernel herding could also be used to quantize conditional distributions, using the conditional kernel mean embedding concept reviewed by [40]. Regarding the industrial use case, the next step is to realize a reliability analysis by considering another group of random variables (related to the wind turbine). Among other ideas, our upcoming work could explore a reliability-oriented sensitivity analysis by adapting recent kernel-based sensitivity indices [50] to the sensitivity of a failure probability.

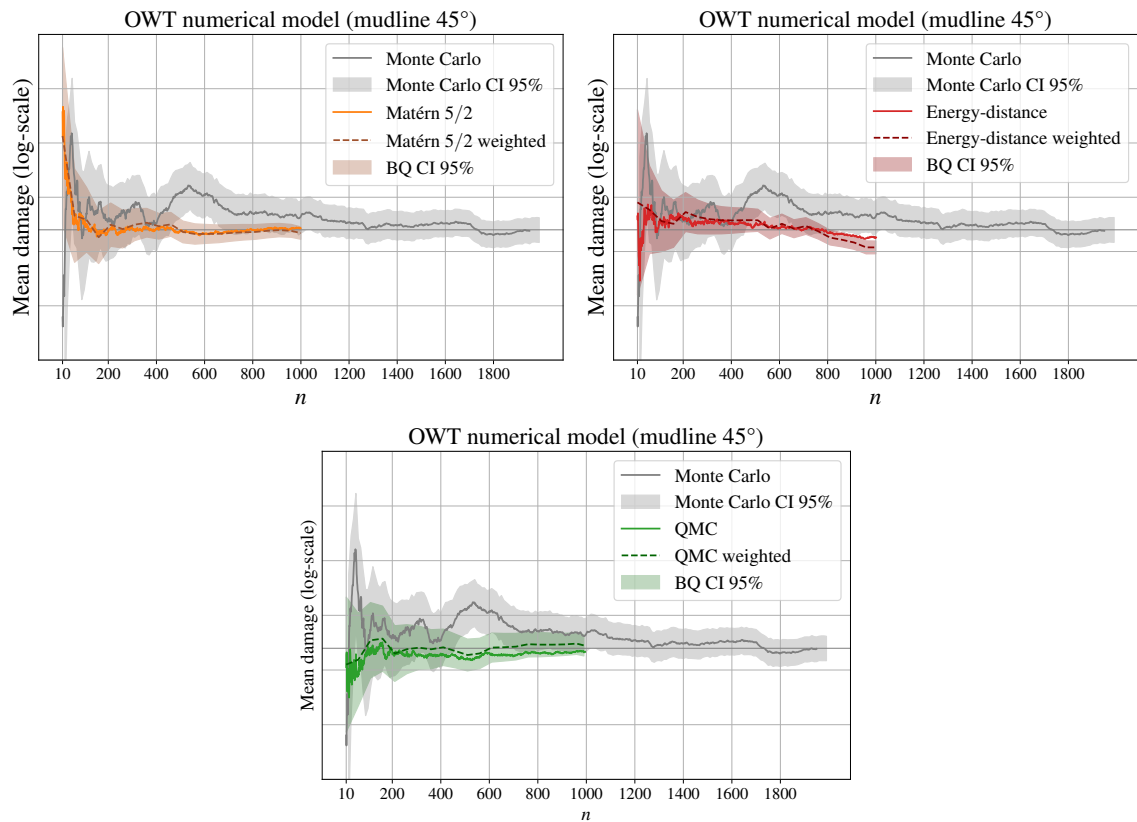


Fig. 4.15 Mean estimation convergence (at the mudline, azimuth  $\theta = 45$  deg.) on the Teesside case

# **Chapter 5**

## **Kernel-based metamodel validation**

**5.1 Introduction**

**5.2 Sequential validation design**

**5.3 Computer experiments context**

**5.4 Machine learning given-data context**

**5.5 Application to wind turbine production metamodel**

**5.6 Conclusion**



## **Part III**

### **Contributions to rare event estimation**



# Chapter 6

## Nonparametric rare event estimation

### 6.1 Introduction

Reliability analysis of a system is often associated with rare event probability estimation. Considering that the system's performance is modeled by a deterministic scalar function  $g : \mathcal{D}_x \subseteq \mathbb{R}^d \rightarrow \mathbb{R}$ , called *limit-state function* and a critical threshold on the system's output  $y_{\text{th}} \in \mathbb{R}$ , one can define the *failure domain* as  $\mathcal{F}_x := \{\mathbf{x} \in \mathcal{D}_x | g(\mathbf{x}) \leq y_{\text{th}}\}$ . Uncertain inputs are represented by a continuous random vector  $\mathbf{X} \in \mathcal{D}_x$  assumed to be distributed according to its joint probability density function (PDF)  $f_{\mathbf{X}}$ . In this context, uncertainty propagation consists in composing the random vector  $\mathbf{X}$  by the function  $g$  to get an output variable of interest  $Y = g(\mathbf{X}) \in \mathbb{R}$ . A usual risk measure in reliability analysis is the *failure probability*, denoted by  $p_f$ , and defined as the probability that the system exceeds the threshold  $y_{\text{th}}$ : Rare event problems are usually solved in the so-called *standard normal space* after applying an “iso-probabilistic transformation” which can be either the Rosenblatt or the generalized Nataf one [46]. Additionally, the limit-state function  $g$  can be viewed as an input-output “black-box” model which can be costly to evaluate (e.g., a complex numerical model), making the failure probability estimation nontrivial. When the limit-state function is a costly computer model, one can build a surrogate model and use specific active learning methods (see, e.g., Moustapha et al. [55]). However, using surrogate models is not always possible for practical engineering applications as they might introduce another level of approximation, which can be prohibitive from safety auditing. Moreover, their validation as well as their behavior with respect to large input dimension case make also their use quite complex (see, e.g., [51]).

Going back to the rare event estimation literature, one can consider two major types of techniques for failure probability calculation [53]: (i) Geometric approaches, such as the *first-/second-order reliability method* (FORM/SORM) whose aim is to approximate the limit-state function by a first-/second-order Taylor expansion at the most probable failure point; (ii) Simulation-based techniques such as the *crude Monte Carlo* method. Unfortunately, FORM/SORM methods do not provide a lot of statistical information as they are purely

geometric approaches. Meanwhile, estimating a rare event probability by crude Monte Carlo becomes rapidly intractable. To overcome this limit, advanced simulation techniques have been developed: among others, one can mention several “variance reduction methods” such as the non-adaptive and adaptive versions of the *Importance Sampling* [67] (either parametric, using the Cross-Entropy method Kurtz and Song [42], or nonparametric Morio [52]) and splitting techniques [9] such as the *Subset Simulation* (SS) Au and Beck [3]. In these techniques, the idea is to write the rare event  $p_f$  as a product of larger conditional probabilities, each one of them being easier to estimate. To generate intermediary conditional samples, this method uses Markov chain Monte Carlo (MCMC) sampling, which presents numerous versions [62]. However, MCMC algorithms are known to be highly tunable algorithms which produce non-i.i.d. samples, which consequently, cannot be used for direct statistical estimation (e.g., failure probability or sensitivity indices [14]).

The present work proposes a new rare event estimation method, adopting the same sequential structure as SS while using a strictly different sampling mechanism to generate conditional samples. This method intends to fit the intermediary conditional distributions with a nonparametric tool called the *Empirical Bernstein Copula*. Contrarily to SS, the proposed method named “Bernstein adaptive nonparametric conditional sampling” (BANCS), generates i.i.d. samples of the intermediary conditional distributions. For instance, a practical use of such i.i.d. samples can be to estimate dedicated reliability-oriented sensitivity indices (see, e.g., [10, 50]).

In this paper, Section 2 will recall the methodology of subset sampling and probabilistic modeling. Then, Section 3 will introduce the BANCS method for rare event estimation. Section 4 will apply this method to three toy-cases and analyze the results with respect to SS performances. Then, the last section present some conclusions and research perspectives.

### 6.1.1 Background

#### Subset sampling

Subset sampling splits the failure event  $\mathcal{F}_x$  into an intersection of  $k_\#$  intermediary events  $\mathcal{F}_x = \cap_{k=1}^{k_\#} \mathcal{F}_{[k]}$ . Each are nested such that  $\mathcal{F}_{[1]} \supset \dots \supset \mathcal{F}_{[k_\#]} = \mathcal{F}_x$ . The failure probability is then expressed as a product of conditional probabilities:

$$p_f = \mathbb{P}(\mathcal{F}_x) = \mathbb{P}(\cap_{k=1}^{k_\#} \mathcal{F}_{[k]}) = \prod_{k=1}^{k_\#} \mathbb{P}(\mathcal{F}_{[k]} | \mathcal{F}_{[k-1]}). \quad (6.1)$$

From a practical point of view, the analyst tunes the algorithm by setting the intermediary probabilities  $\mathbb{P}(\mathcal{F}_{[k]} | \mathcal{F}_{[k-1]}) = p_0, \forall k \in \{1, \dots, k_\#\}$ . Then, the corresponding quantiles  $q_{[1]}^{p_0} > \dots > q_{[k_\#]}^{p_0}$  are estimated for each conditional subset samples  $\mathbf{X}_{[k],N}$  of size  $N$ . Note that the initial quantile is estimated by crude Monte Carlo sampling on the input PDF  $f_X$ . Following conditional subset samples are generated by MCMC sam-

pling of  $f_{\mathbf{X}}(\mathbf{x}|\mathcal{F}_{[k-1]})$ , using as seeds initialisation points the  $n = Np_0$  samples given by  $\mathbf{A}_{[k],n} = \{\mathbf{X}_{[k-1]}^{(j)} \subset \mathbf{X}_{[k-1],N} | g(\mathbf{X}_{[k-1]}^{(j)}) > \hat{q}_{[k-1]}^{\alpha}\}_{j=1}^n$ . This process is repeated until an intermediary quantile exceeds the threshold:  $\hat{q}_{[k\#]}^{p_0} < y_{\text{th}}$ . Finally, the failure probability is estimated by:

$$p_f \approx \hat{p}_f^{\text{SS}} = p_0^{k\#-1} \frac{1}{N} \sum_{j=1}^N \mathbb{1}_{\{g(\mathbf{x}) \leq y_{\text{th}}\}} (\mathbf{X}_{[k\#],N}^{(j)}). \quad (6.2)$$

In practice, the subset sample size should be large enough to properly estimate intermediary quantiles, which leads [3] to recommend setting  $p_0 = 0.1$ . SS efficiency depends on the proper choice and tuning of the MCMC algorithm [62]. Our work uses the SS implementation from OpenTURNS<sup>1</sup> [5] which integrates a component-wise Metropolis-Hastings algorithm. As an alternative to generating samples on a conditional distribution by MCMC, one could try to fit this conditional distribution.

### Multivariate modeling using copulas

The Sklar theorem [31] affirms that the multivariate distribution of any random vector  $\mathbf{X} \in \mathbb{R}^d$  can be broken down into two objects:

1. A set of univariate marginal distributions to describe the behavior of the individual variables;
2. A function describing the dependence structure between all variables, called a copula.

This theorem states that considering a random vector  $\mathbf{X} \in \mathbb{R}^d$ , with its distribution  $F$  and its marginals  $\{F_i\}_{i=1}^d$ , there exists a copula  $C : [0, 1]^d \rightarrow [0, 1]$ , such that:

$$F(x_1, \dots, x_d) = C(F_1(x_1), \dots, F_p(x_d)). \quad (6.3)$$

It allows us to divide the problem of fitting a joint distribution into two independent problems: fitting the marginals and fitting the copula. Note that when the joint distribution is continuous, this copula is unique. Provided a dataset, this framework allows to combine a parametric (or nonparametric) fit of marginals with a parametric (or nonparametric) fit of the copula. When the distribution's dimension is higher than two, one can perform a parametric fit using vine copulas [32], implying the choice of multiple types of parametric copulas. Otherwise, nonparametric fit by multivariate kernel density estimation (KDE) presents a computational burden as soon as the dimension increases [10]. Since univariate marginals are usually well-fitted with nonparametric tools (e.g., KDE), let us introduce an effective nonparametric method for copula fitting.

---

<sup>1</sup><https://openturns.github.io/www/index.html>

## 6.2 Bernstein adaptive nonparametric conditional sampling

### 6.2.1 Empirical Bernstein copula

Copulas are continuous and bounded functions defined on a compact set (the unit hypercube). Bernstein polynomials allow to uniformly approximate as closely as desired any continuous and real-valued function defined on a compact set (Weierstrass approximation theorem). Therefore, they are good candidates to approximate unknown copulas. This concept was introduced as *empirical Bernstein copula* (EBC) by [68] for applications in economics and risk management. Later on, [69] offered further asymptotic studies. Formally, the multivariate Bernstein polynomial for a function  $C : [0, 1]^d \rightarrow \mathbb{R}$  on a grid over the unit hypercube  $G := \left\{ \frac{0}{m_1}, \dots, \frac{m_1}{m_1} \right\} \times \dots \times \left\{ \frac{0}{m_d}, \dots, \frac{m_d}{m_d} \right\}, \mathbf{m} = (m_1, \dots, m_d) \in \mathbb{N}^d$ , writes:

$$B_{\mathbf{m}}(C)(\mathbf{u}) := \sum_{t_1=0}^{m_1} \dots \sum_{t_d=0}^{m_d} C\left(\frac{t_1}{m_1}, \dots, \frac{t_d}{m_d}\right) \prod_{j=1}^d P_{m_j, t_j}(u_j), \quad (6.4)$$

with  $\mathbf{u} = (u_1, \dots, u_d) \in [0, 1]^d$ , and the Bernstein polynomial  $P_{m, t}(u) := \frac{t!}{m!(t-m)!} u^m (1-u)^{t-m}$ . Notice how the grid definition implies the polynomial's order. When  $C$  is a copula, then  $B_{\mathbf{m}}(C)$  is called “Bernstein copula”. Therefore, the empirical Bernstein copula is an application of the Bernstein polynomial in Eq. (6.4) to the so-called “empirical copula”.

In practice, considering a sample  $\mathbf{X}_n = \left\{ \mathbf{x}^{(1)}, \dots, \mathbf{x}^{(n)} \right\} \in \mathbb{R}^{np}$  and the associated ranked sample  $\mathbf{R}_n = \left\{ \mathbf{r}^{(1)}, \dots, \mathbf{r}^{(n)} \right\}$ , the corresponding empirical copula writes:

$$C_n(\mathbf{u}) := \frac{1}{n} \sum_{i=0}^n \prod_{j=1}^p \mathbb{1} \left\{ \frac{r_j^{(i)}}{n} \leq u_j \right\}, \quad (6.5)$$

with  $\mathbf{u} = (u_1, \dots, u_d) \in [0, 1]^d$ . In the following, the polynomial order is set as equal in each dimension:  $\{m_i = m\}_{j=1}^d$ . Theoretically, the tuning parameter can be optimized to minimize an “Mean Integrated Squared Error” (MISE), leading to a bias-variance tradeoff. Formally, the MISE of the empirical Bernstein copula  $B_{\mathbf{m}}(C_n)$  is defined as follows:

$$\mathbb{E} [\|B_{\mathbf{m}}(C_n) - C\|_2^2] = \mathbb{E} \left[ \int_{\mathbb{R}^d} (B_{\mathbf{m}}(C_n)(\mathbf{u}) - C(\mathbf{u}) d\mathbf{u})^2 \right]. \quad (6.6)$$

Then, [68] prove in their Theorem 3 that:

- $B_{\mathbf{m}}(C_n)(\mathbf{u}) \rightarrow C(\mathbf{u})$  for any  $u_j \in ]0, 1[$  if  $\frac{m^{d/2}}{n} \rightarrow 0$ , when  $m, n \rightarrow \infty$ .
- The optimal order of the polynomial in terms of MISE is:  $m \lesssim m_{\text{IMSE}} = n^{2/(d+4)}$ ,  $\forall u_j \in ]0, 1[$ . The sign  $\lesssim$  means “less than or approximately”.

Let us remark that in the special case  $m = n$ , also called the “Beta copula” in [69], the bias is very small while the variance gets large. To illustrate the previous theorem,

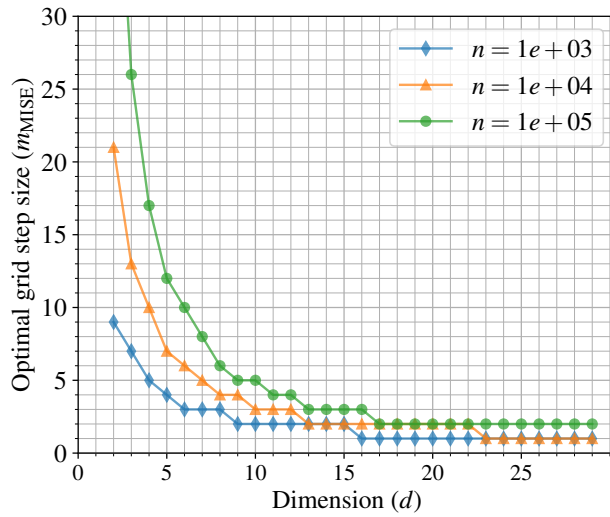


Fig. 6.1 Evolution of  $m_{IMSE}$  for different dimensions and sample sizes.

[44] represents the evolution of the  $m_{IMSE}$  for different dimensions and sample sizes (see Fig. 6.1). In high dimension, the values of  $m_{IMSE}$  tend towards one, which is equivalent to the independent copula. Therefore, high-dimensional problems should be divided into a product of smaller problems on which the EBC is tractable. Provided a large enough learning set  $\mathbf{X}_n$ , KDE fitting of marginals combined with EBC fitting of the copula delivers good results even on complex dependence structures. Moreover, EBC provides an explicit expression, making a Monte Carlo generation of i.i.d. samples simple. In the following, this nonparametric tool is used to fit the intermediary conditional distributions present in subset sampling.

### 6.2.2 Bernstein adaptive nonparametric conditional sampling algorithm

This new method reuses the main idea from SS while employing a different approach to generate conditional samples. Instead of using MCMC sampling, the conditional distribution is firstly fitted by a nonparametric procedure, before sampling on this nonparametric model. As described in Algorithm 1, conditional sampling is done on a distribution composed by merging marginals  $\{\widehat{F}_i\}_{i=1}^d$  fitted by KDE, with a copula  $B_m(C_n)$  fitted by EBC. Fig. 6.2 illustrate the nonparametric fit and conditional sampling in BANCS method on a two-dimensional reliability problem (later introduced as “toy-case #1”). At iteration  $k$ , after estimating the intermediary quantile  $\widehat{q}_{[k]}^{p_0}$ , a nonparametric model is fitted on  $\mathbf{A}_{[k+1],n}$  and used to generate the next  $N$ -sized subset sample  $\mathbf{X}_{[k+1],N}$ . Note that the BANCS method does not require iso-probabilistic transform.

As discussed in the previous section, EBC fitting is tuned by the Bernstein polynomial of order  $m$ , implying a bias-variance tread off. In Fig. 6.2, conditional distributions fitted by EBC (blue and brown isolines) seem to present a slight bias since they overlay the

**Algorithm 1** Bernstein adaptive nonparametric conditional sampling (BANCS).

▷ *Inputs:*

- $f_{\mathbf{X}}$ , joint PDF of the inputs
- $g(\cdot)$ , limit-state function
- $y_{\text{th}} \in \mathbb{R}$ , threshold defining the failure event
- $N$ , number of samples per iteration
- $m \in \mathbb{N}$ , parameter of the EBC fitting
- $p_0 \in ]0, 1[$ , empirical quantile order (rarity parameter)

▷ *Algorithm:*

- Set  $k = 0$  and  $f_{[0]} = f_{\mathbf{X}}$
- Sample  $\mathbf{X}_{[0],N} = \{\mathbf{X}_{[0]}^{(j)}\}_{j=1}^N \stackrel{\text{i.i.d.}}{\sim} f_{[0]}$
- Evaluate  $G_{[0],N} = \{g(\mathbf{X}_{[0]}^{(j)})\}_{j=1}^N$
- Estimate the empirical  $p_0$ -quantile  $\hat{q}_{[0]}^{p_0}$  of the set  $G_{[0],N}$
- while**  $\hat{q}_{[k]}^{p_0} > y_{\text{th}}$  **do**

  - Subsample  $\mathbf{A}_{[k+1],n} = \{\mathbf{X}_{[k]}^{(j)} \subset \mathbf{X}_{[k],N} | g(\mathbf{X}_{[k]}^{(j)}) > \hat{q}_{[k]}^{p_0}\}_{j=1}^n$
  - Fit marginals of the subset  $\mathbf{A}_{[k+1],n}$  by KDE  $\{\hat{F}_i\}_{i=1}^d$
  - Fit the copula of the subset  $\mathbf{A}_{[k+1],n}$  by EBC  $B_m(C_n)$
  - Build a CDF  $\hat{F}_{[k+1]}(\mathbf{x}) = B_m(C_n)(\hat{F}_1(x_1), \dots, \hat{F}_d(x_d))$
  - Sample  $\mathbf{X}_{[k+1],N} = \{\mathbf{X}_{[k+1]}^{(j)}\}_{j=1}^N \stackrel{\text{i.i.d.}}{\sim} \hat{f}_{[k+1]}$
  - Evaluate  $G_{[k+1],N} = \{g(\mathbf{X}_{[k+1]}^{(j)})\}_{j=1}^N$
  - Estimate the empirical  $p_0$ -quantile  $\hat{q}_{[k+1]}^{p_0}$  of  $G_{[k+1],N}$
  - Set  $k = k + 1$

- Set total iteration number  $k_{\#} = k - 1$
- Estimate  $\hat{p}_f = (1 - p_0)^{k_{\#}} \cdot \frac{1}{N} \sum_{j=1}^N \mathbb{1}_{\{g(\mathbf{X}_{[k_{\#}]^{(j)}}) \geq y_{\text{th}}\}} (\mathbf{X}_{[k_{\#}]^{(j)}})$

▷ *Outputs:*

$\hat{p}_f$ , estimate of  $p_f$

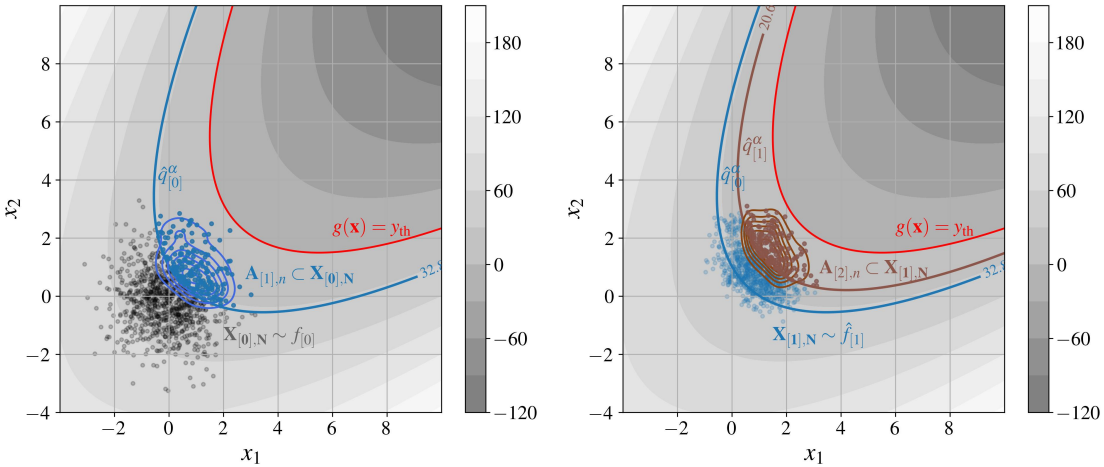


Fig. 6.2 BANCS on toy-case #1: illustration of conditional sampling and nonparametric fit at the first and second iterations.

quantiles. However, reducing this bias implies decreasing the tuning parameter  $m$ , until  $m = 1$ , which is equivalent to an independent copula. Tools to control the goodness of fit of nonparametric conditional distributions are also available. As an example, let us consider the fitted conditional distribution at the first iteration (visible in Fig. 6.2). Its

quantile-quantile plot in Fig. 6.3 shows a good fit of the two marginals by KDE. Then, the goodness of fit of copulas can be evaluated by Kendall's plot, represented in Fig. 6.4. This fit is also good, even if a slight bias is again visible.

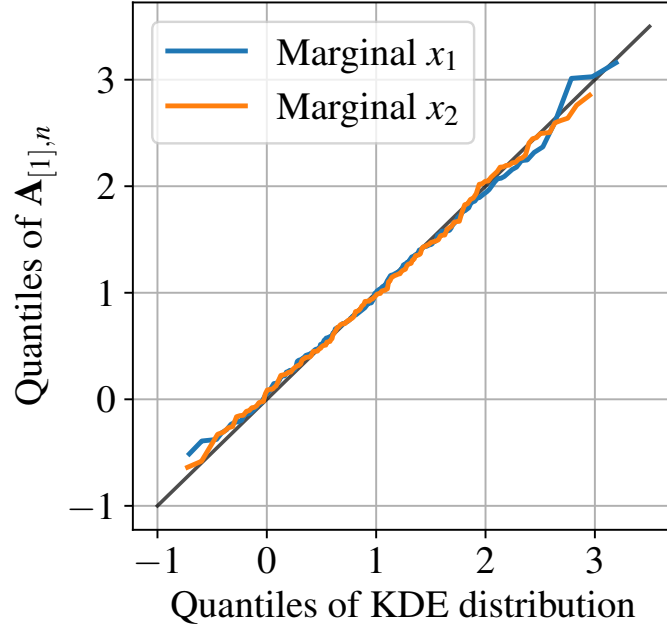


Fig. 6.3 QQ-plot for KDE of marginals of the conditional distribution from Fig. 6.2.

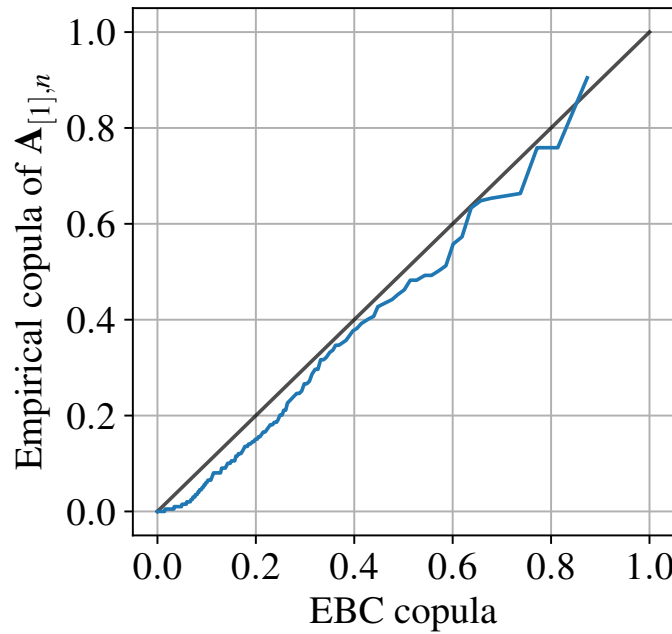


Fig. 6.4 Kendall plot for EBC on the copula of a conditional distribution from Fig. 6.2.

### 6.3 Numerical experiments

In the following analytical numerical experiments, the intermediary probabilities were set to  $p_0 = 0.1$ , allowing a fair comparison with subset sampling. Then, the subset sample size is set to  $N = 10^4$ , in order to get a reasonable sample size  $n = Np_0 = 10^3$  to perform the nonparametric fitting. EBC tuning is setup to minimize the MISE in Eq. (6.6):  $m = 1 + n^{\frac{2}{d+4}}$ . In order to take into account the variability of the method's results, each experiment is repeated 100 times, allowing the computation of a coefficient of variation  $\hat{\delta} = \frac{\sigma_{\hat{p}_f}}{\mu_{\hat{p}_f}}$ . Note that an implementation of the BANCS method and the following numerical experiments are available in a Git repository<sup>2</sup>.

**Toy-case #1: Parabolic reliability problem** Let us define the parabolic reliability problem, considering the function  $g_1 : \mathbb{R}^2 \rightarrow \mathbb{R}$ :

$$g_1(\mathbf{x}) = (x_1 - x_2)^2 - 8(x_1 + x_2 - 5), \quad (6.7)$$

with the input random vector  $\mathbf{X} = (X_1, X_2)$  following a standard 2-dimensional normal distribution. The reliability problem consists in evaluating:  $p_{f,1} = \mathbb{P}(g_1(\mathbf{X}) \leq 0) = 1.31 \times 10^{-4}$ .

**Toy-case #2: Four-branch reliability problem** Let us define the four-branch reliability problem (originally proposed by [79]), considering the following function  $g_2 : \mathbb{R}^2 \rightarrow \mathbb{R}$ :

$$g_2(\mathbf{x}) = \min \left( \begin{array}{l} 5 + 0.1(x_1 - x_2)^2 - \frac{(x_1 + x_2)}{\sqrt{2}} \\ 5 + 0.1(x_1 - x_2)^2 + \frac{(x_1 + x_2)}{\sqrt{2}} \\ (x_1 - x_2) + \frac{9}{\sqrt{2}} \\ (x_2 - x_1) + \frac{9}{\sqrt{2}} \end{array} \right), \quad (6.8)$$

with the input random vector  $\mathbf{X} = (X_1, X_2)$  following a standard 2-dimensional normal distribution. The reliability problem consists in evaluating:  $p_{f,2} = \mathbb{P}(g_2(\mathbf{X}) \leq 0) = 2.21 \times 10^{-4}$ .

**Toy-case #3: high-dimensional reliability problem** Let us define the higher-dimensional reliability problem (proposed by [81]), considering the following function  $g_3 : \mathbb{R}^7 \rightarrow \mathbb{R}$ :

$$g_3(\mathbf{x}) = 15.59 \times 10^4 - \frac{x_1 x_3^2}{2x_3^2} \frac{x_2^4 - 4x_5 x_6 x_7^2 + x_4(x_6 + 4x_5 + 2x_6 x_7)}{x_4 x_5(x_4 + x_6 + 2x_6 x_7)}, \quad (6.9)$$

---

<sup>2</sup><https://github.com/efekhari27/icasp14>

with the input random vector  $\mathbf{X} = (X_1, \dots, X_7)$ , following a product of normal distributions defined in [81]. The reliability problem consists in evaluating:  $p_{f,3} = \mathbb{P}(g_3(\mathbf{X}) \leq 0) = 8.10 \times 10^{-3}$ .

### 6.3.1 Results analysis

Results of our numerical experiments are presented graphically (for 2-dimensional problems) in Figures 6.5 and 6.6, and numerically in Table 6.1. In the same fashion as the previous illustrations, the figures represent the intermediary quantiles  $\hat{q}_{[k]}^{p_0}$  estimated over conditional samples of size  $N = 10^4$ . Moreover, samples  $\mathbf{A}_{[k+1],n}$  exceeding these quantiles are also represented in the same color. Notice how the last estimated quantile is set to the problem threshold  $y_{\text{th}} = 0$ . To capture the dispersion of BANCS estimation, 100 repetitions were realized. Let us notice that for each toy-case, BANCS well estimates the failure probabilities' orders of magnitude. Yet the numerical values in Table 6.1 consistently present a positive bias, leading to an overestimated failure probability. This bias is partially explained by the EBC tuning choice and could be reduced at the expense of a slightly higher variance.

The variance obtained with the repetitions is quite large. Although, part of it is due to the fact that the algorithm might compute a different total number of subsets (e.g., toy-case #1 is either solved in four or five subsets). Overall, considering the EBC tuning from Eq. (6.6), BANCS performs worst than SS on toy-cases #1 and #2 but performs as well as SS on the toy-case #3. This might be due to the fact that toy-case #3 has a higher input dimension. However, one can note that SS coefficient of variation is computed by an approximation, tending to underestimate the true coefficient of variation (see e.g., [62]).

Table 6.1 Results of the numerical experiments (subset sample size  $N = 10^4$ ,  $p_0 = 0.1$ ).

	$d$	$p_f^{\text{ref}}$	$\hat{p}_f^{\text{BANCS}}$	$\hat{\delta}^{\text{BANCS}}$	$\hat{p}_f^{\text{SS}}$	$\hat{\delta}^{\text{SS}}$
Toy-case #1	2	$1.31 \times 10^{-4}$	$2.67 \times 10^{-4}$	24%	$1.30 \times 10^{-4}$	9%
Toy-case #2	2	$2.21 \times 10^{-4}$	$4.23 \times 10^{-4}$	7%	$2.24 \times 10^{-4}$	6%
Toy-case #3	7	$8.10 \times 10^{-3}$	$9.32 \times 10^{-3}$	15%	$8.92 \times 10^{-3}$	6%

## 6.4 Application to wind turbine fatigue reliability

### 6.5 Conclusion

Subset Simulation uses MCMC sampling to generate its intermediary conditional samples. However, MCMC algorithms tends to be complex to tune and does not generate i.i.d. conditional samples. In this work, a new method is proposed, replacing MCMC sampling with a simpler procedure. An intermediary conditional distribution is first fitted by a nonparametric approach, mixing kernel density estimation for fitting the marginals and

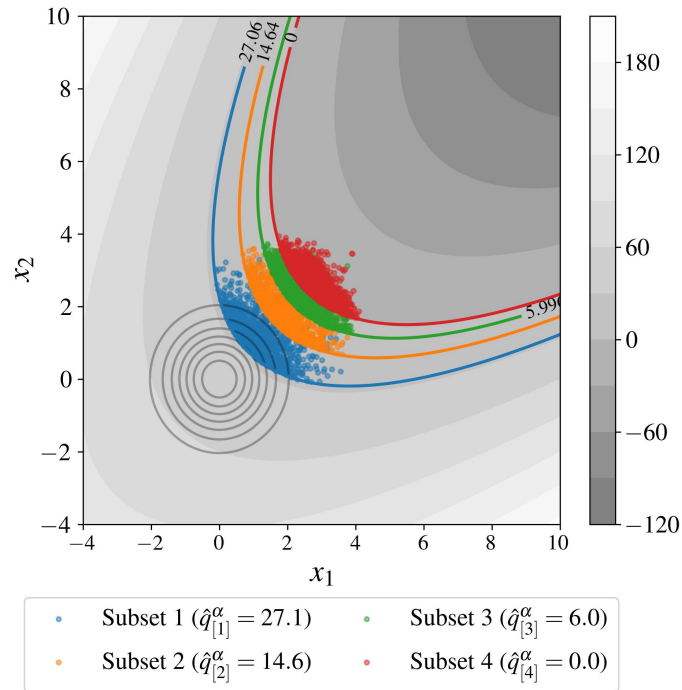


Fig. 6.5 BANCS sampling steps on toy-case #1.

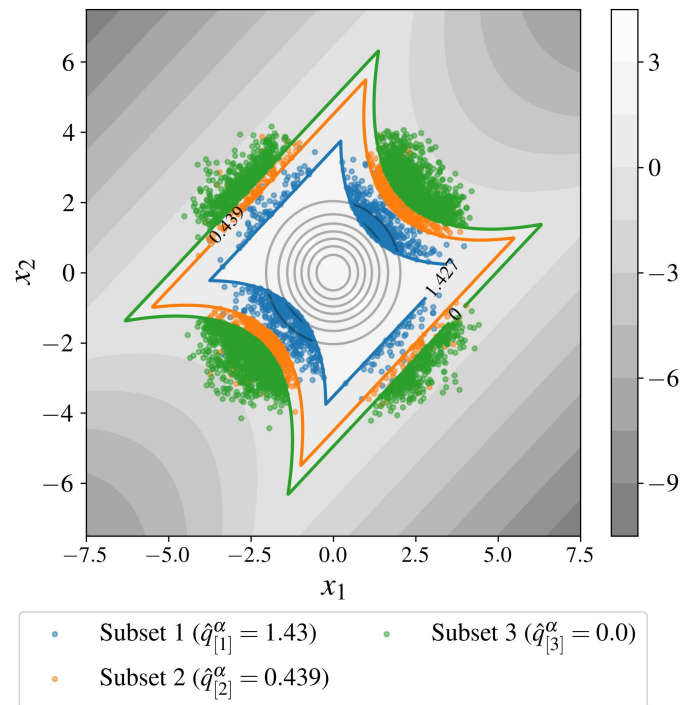


Fig. 6.6 BANCS sampling steps on toy-case #2.

Empirical Bernstein Copula (EBC) for fitting the copula. Then, the resulting allows to perform direct Monte Carlo sampling. This method is named “Bernstein adaptive nonparametric conditional sampling” (BANCS) and is applied to three toy-cases (two 2-dimensional and one 7-dimensional) and compared with SS.

The method shows promising results, even though a small positive bias consistently appears. This issue results from EBC tuning, creating a bias-variance tradeoff in the copula fit. Theoretical works offer optimal tuning, allowing us to find the optimal compromise. In our numerical experiments, an empirical estimation of BANCS variance is computed over a set of repetitions. BANCS estimated coefficient of variation is higher than SS approximated coefficient of variation. This work can be further explored by building an approximation of BANCS variance and confidence interval. One major advantage remains that the samples generated at each iteration are i.i.d. leading to a possible use of these samples to perform global reliability-oriented sensitivity analysis [50] in order to detect and analyze the most influential input variables leading to failure.



# **Chapter 7**

## **Sequential reliability oriented sensitivity analysis**

**7.1 Conclusion**

**7.2 HSIC for GSA**

**7.3 HSIC for TSA & CSA**

**7.4 Sequential ROSA**

**7.5 Application to wind turbine fatigue reliability**

**7.6 Conclusion**



## **Conclusion and perspectives**



# References

- [1] Abdallah, I., Lataniotis, C., and Sudret, B. (2019). Parametric hierarchical kriging for multi-fidelity aero-servo-elastic simulators – Application to extreme loads on wind turbines. *Probabilistic Engineering Mechanics*, 55:67 – 77.
- [2] Ajenjo, A. (2023). *Info-gap robustness assessment of reliability evaluations for the safety of critical industrialsystems*. PhD thesis, Université Bourgogne Franche-Comté.
- [3] Au, S.-K. and Beck, J. L. (2001). Estimation of small failure probabilities in high dimensions by subset simulation. *Probabilistic Engineering Mechanics*, 16(4):263–277.
- [4] Bai, H., Shi, L., Aoues, Y., Huang, C., and Lemosse, D. (2023). Estimation of probability distribution of long-term fatigue damage on wind turbine tower using residual neural network. *Mechanical Systems and Signal Processing*, 190:110101.
- [5] Baudin, M., Dutfoy, A., Iooss, B., and Popelin, A. (2017). Open TURNS: An industrial software for uncertainty quantification in simulation. In Ghanem, R., Higdon, D., and Owhadi, H., editors, *Springer Handbook on Uncertainty Quantification*, pages 2001–2038. Springer.
- [6] Briol, F., Oates, C., Girolami, M., Osborne, M., and Sejdinovic, D. (2019). Probabilistic Integration: A Role in Statistical Computation? *Statistical Science*, 34:1 – 22.
- [7] Briol, F.-X. (2019). *Statistical computation with kernels*. PhD thesis, University of Warwick.
- [8] Briol, F.-X., Oates, C., Girolami, M., and Osborne, M. (2015). Frank-Wolfe Bayesian Quadrature: Probabilistic Integration with Theoretical Guarantees. In *Advances in Neural Information Processing Systems*.
- [9] Cérou, F., Del Moral, P., Furon, T., and Guyader, A. (2012). Sequential monte carlo for rare event estimation. *Statistics and computing*, 22:795–808.
- [10] Chabridon, V., Balesdent, M., Perrin, G., Morio, J., Bourinet, J.-M., and Gayton, N. (2021). Global reliability-oriented sensitivity analysis under distribution parameter uncertainty. *Mechanical Engineering under Uncertainties: From Classical Approaches to Some Recent Developments*, pages 237–277.
- [11] Chen, T., Wang, X., Yuan, G., and Liu, J. (2018). Fatigue bending test on grouted connections for monopile offshore wind turbines. *Marine Structures*, 60:52–71.
- [12] Chen, Y., Welling, M., and Smola, A. (2010). Super-samples from kernel herding. In *Proceedings of the Twenty-Sixth Conference on Uncertainty in Artificial Intelligence*, pages 109 – 116. AUAI Press.
- [13] Da Veiga, S. (2015). Global sensitivity analysis with dependence measures. *Journal of Statistical Computation and Simulation*, 85:1283 – 1305.

- [14] Da Veiga, S., Gamboa, F., Iooss, B., and Prieur, C. (2021). *Basics and Trends in Sensitivity Analysis: Theory and Practice in R*. Society for Industrial and Applied Mathematics.
- [15] de Rocquigny, E., Devictor, N., and Tarantola, S. (2008). *Uncertainty in industrial practice: a guide to quantitative uncertainty management*. John Wiley & Sons.
- [16] Dimitrov, N., Kelly, M., Vignaroli, A., and Berg, J. (2018). From wind to loads: wind turbine site-specific load estimation with surrogate models trained on high-fidelity load databases. *Wind Energy Science*, 3:767 – 790.
- [17] DNV-GL (2016a). DNVGL-RP-C203: Fatigue design of offshore steel structures. Technical report, DNVGL.
- [18] DNV-GL (2016b). DNVGL-ST-0437: Loads and site conditions for wind turbines. Technical report, DNVGL.
- [19] Dowling, N. E. (1972). Fatigue Failure Predictions for Complicated Stress-Strain Histories. *Journal of Materials, JMSA*, 7:71 – 87.
- [20] Fatemi, A. and Yang, L. (1998). Cumulative fatigue damage and life prediction theories: a survey of the state of the art for homogeneous materials. *International Journal of Fatigue*, 20(1):9–34.
- [21] Fekhari, E., Chabridon, V., Mure, J., and Iooss, B. (2023a). Bernstein adaptive non-parametric conditional sampling: a new method for rare event probability estimation. preprint: hal-04052861v1.
- [22] Fekhari, E., Iooss, B., Muré, J., Pronzato, L., and Rendas, J. (2023b). Model predictivity assessment: incremental test-set selection and accuracy evaluation. In Salvati, N., Perna, C., Marchetti, S., and Chambers, R., editors, *Studies in Theoretical and Applied Statistics*, pages 315–347. Springer.
- [23] Fuhr, J., Fau, A., and Nackenhorst, U. (2021). State-of-the-Art and Comparative Review of Adaptive Sampling Methods for Kriging. *Archives of Computational Methods in Engineering*, 28:2689–2747.
- [24] Graf, P., Stewart, G., Lackner, M., Dykes, K., and Veers, P. (2016). High-throughput computation and the applicability of Monte Carlo integration in fatigue load estimation of floating offshore wind turbines. *Wind Energy*, 19(5):861–872.
- [25] Gretton, A., Borgwardt, K. M., Rasch, M., Schölkopf, B., and Smola, A. (2006). A Kernel Method for the Two-Sample-Problem. In *Proceedings of the 19th International Conference on Neural Information Processing Systems*, pages 513–520.
- [26] Hansen, M. and Henriksen, L. (2013). *Basic DTU Wind Energy controller*. Number 0028 in DTU Wind Energy E. DTU Wind Energy.
- [27] Huchet, Q. (2019). *Kriging based methods for the structural damage assessment of offshore wind turbines*. PhD thesis, Université Blaise Pascal.
- [28] Huchet, Q., Matstrand, C., Beaurepaire, P., Relun, N., and Gayton, N. (2019). AK-DA: An efficient method for the fatigue assessment of wind turbine structures. *Wind Energy*, 22(5):638–652.
- [29] Huszár, F. and Duvenaud, D. (2012). Optimally-Weighted Herding is Bayesian Quadrature. In *Proceedings of the Twenty-Eighth Conference on Uncertainty in Artificial Intelligence*, pages 377 – 386.

- [30] IEC (2019). IEC 61400-1: Wind energy generation systems - Part 1: Design requirements. Technical report, International Electrotechnical Commission (IEC).
- [31] Joe, H. (1997). *Multivariate Models and Multivariate Dependence Concepts*. Chapman and Hall.
- [32] Joe, H. and Kurowicka, D. (2011). *Dependence modeling: vine copula handbook*. World Scientific.
- [33] Jonkman, B. (2009). Turbsim User's Guide: Version 1.50. Technical report, NREL.
- [34] Kaimal, J., Wyngaard, J., Izumi, Y., and Coté, O. (1972). Spectral characteristics of surface-layer turbulence. *Quarterly Journal of the Royal Meteorological Society*, 98(417):563–589.
- [35] Kanagawa, M. and Hennig, P. (2019). Convergence Guarantees for Adaptive Bayesian Quadrature Methods. In *Advances in Neural Information Processing Systems*, volume 32.
- [36] Kanagawa, M., Hennig, P., Sejdinovic, D., and Sriperumbudur, B. (2018). Gaussian Processes and Kernel Methods: A Review on Connections and Equivalences. preprint.
- [37] Kaplan, Z., Li, Y., Nakayama, M., and Tuffin, B. (2019). Randomized quasi-Monte Carlo for quantile estimation. In *2019 Winter Simulation Conference (WSC)*, pages 428–439.
- [38] Kelly, M. and Vanem, E. (2022). Environmental joint probability distributions and uncertainties. Technical report, Tech Rep. of HIPERWIND H2020 project, Grant Agreement No. 101006689, <https://www.hiperwind.eu/>.
- [39] Kim, T., Natarajan, A., Lovera, A., Julian, E., Peyrard, E., Capaldo, M., Huwart, G., Bozonnet, P., and Guiton, M. (2022). A comprehensive code-to-code comparison study with the modified IEA15MW-UMaine Floating Wind Turbine for H2020 HIPERWIND project. *Journal of Physics: Conference Series*, 2265(4):042006.
- [40] Klebanov, I., Schuster, I., and Sullivan, T. (2020). A rigorous theory of conditional mean embeddings. *SIAM Journal on Mathematics of Data Science*, 2(3):583–606.
- [41] Kucherenko, S., Feil, B., Shah, N., and Mauntz, W. (2011). The identification of model effective dimensions using global sensitivity analysis. *Reliability Engineering & System Safety*, 96:440–449.
- [42] Kurtz, N. and Song, J. (2013). Cross-entropy-based adaptive importance sampling using Gaussian mixture. *Structural Safety*, 42:35–44.
- [43] Lacoste-Julien, S., Lindsten, F., and Bach, F. (2015). Sequential Kernel Herding: Frank-Wolfe Optimization for Particle Filtering. In *Proceedings of the Eighteenth International Conference on Artificial Intelligence and Statistics*, volume 38, pages 544–552.
- [44] Lasserre, M. (2022). *Apprentissages dans les réseaux bayésiens à base de copules non-paramétriques*. PhD thesis, Sorbonne Université.
- [45] Lataniotis, C. (2019). *Data-driven uncertainty quantification for high-dimensional engineering problems*. PhD thesis, ETH Zürich.
- [46] Lebrun, R. (2013). *Contributions à la modélisation de la dépendance stochastique*. PhD thesis, Université Paris-Diderot – Paris VII. (in English).

- [47] Lebrun, R. and Dutfoy, A. (2009). A generalization of the Nataf transformation to distributions with elliptical copula. *Probabilistic Engineering Mechanics*, 24(2):172–178.
- [48] Li, X. and Zhang, W. (2020). Long-term fatigue damage assessment for a floating offshore wind turbine under realistic environmental conditions. *Renewable Energy*, 159:570–584.
- [49] Mak, S. and Joseph, V. (2018). Support points. *The Annals of Statistics*, 46:2562 – 2592.
- [50] Marrel, A. and Chabridon, V. (2021). Statistical developments for target and conditional sensitivity analysis: Application on safety studies for nuclear reactor. *Reliability Engineering & System Safety*, 214:107711.
- [51] Marrel, A., Iooss, B., and Chabridon, V. (2022). The ICSCREAM methodology: Identification of penalizing configurations in computer experiments using screening and metamodel – Applications in thermal-hydraulics. *Nuclear Science and Engineering*, 196:301–321.
- [52] Morio, J. (2011). Non-parametric adaptive importance sampling for the probability estimation of a launcher impact position. *Reliability Engineering and System Safety*, 96(1):178–183.
- [53] Morio, J. and Balesdent, M. (2015). *Estimation of Rare Event Probabilities in Complex Aerospace and Other Systems: A Practical Approach*. Woodhead Publishing, Elsevier.
- [54] Morokoff, W. J. and Caflisch, R. E. (1995). Quasi-Monte Carlo Integration. *Journal of Computational Physics*, 122(2):218–230.
- [55] Moustapha, M., Marelli, S., and Sudret, B. (2022). Active learning for structural reliability: Survey, general framework and benchmark. *Structural Safety*, 96:102174.
- [56] Murcia, J., Réthoré, P., Dimitrov, N., Natarajan, A., Sørensen, J., Graf, P., and Kim, T. (2018). Uncertainty propagation through an aeroelastic wind turbine model using polynomial surrogates. *Renewable Energy*, 119:910–922.
- [57] Müller, K. and Cheng, P. (2018). Application of a Monte Carlo procedure for probabilistic fatigue design of floating offshore wind turbines. *Wind Energy Science*, 3:149 – 162.
- [58] Nagler, T., Schellhase, C., and Czado, C. (2017). Nonparametric estimation of simplified vine copula models: comparison of methods. *Dependence Modeling*, 5:99–120.
- [59] Oates, C. J. (2021). Minimum Discrepancy Methods in Uncertainty Quantification. Lecture Notes at École Thématische sur les Incertitudes en Calcul Scientifique (ETICS21), <https://www.gdr-mascotnum.fr/etics.html>.
- [60] O'Hagan, A. (1991). Bayes-Hermite quadrature. *Journal of Statistical Planning and Inference*, 29:245–260.
- [61] Owen, A. (2003). The dimension distribution and quadrature test functions. *Statistica Sinica*, 13:1–17.
- [62] Papaioannou, I., Betz, W., Zwirglmaier, K., and Straub, D. (2015). MCMC algorithms for Subset Simulation. *Probabilistic Engineering Mechanics*, 41:89–103.
- [63] Petrovska, E. (2022). *Fatigue life reassessment of monopile-supported offshore wind turbine structures*. PhD thesis, University of Edinburgh.

- [64] Pronzato, L. and Rendas, M. (2021). Validation design I: construction of validation designs via kernel herding. preprint, <https://arxiv.org/abs/2112.05583>.
- [65] Pronzato, L. and Zhigljavsky, A. (2020). Bayesian quadrature and energy minimization for space-filling design. *SIAM/ASA Journal on Uncertainty Quantification*, 8:959 – 1011.
- [66] Rasmussen, C. and Williams, C. (2006). *Gaussian Processes for Machine Learning*. MIT Press.
- [67] Rubinstein, R. Y. and Kroese, D. P. (2008). *Simulation and the Monte Carlo Method*. Wiley, Second ed. edition.
- [68] Sancetta, A. and Satchell, S. (2004). The Bernstein copula and its applications to modeling and approximations of multivariate distributions. *Econometric Theory*, 20(3):535–562.
- [69] Segers, J., Sibuya, M., and Tsukahara, H. (2017). The empirical beta copula. *Journal of Multivariate Analysis*, 155:35–51.
- [70] Sejdinovic, D., Sriperumbudur, B., Gretton, A., and Fukumizu, K. (2013). Equivalence of distance-based and RKHS-based statistics in hypothesis testing. *The Annals of Statistics*, 41:2263–2291.
- [71] Slot, R. M., Sørensen, J. D., Sudret, B., Svenningsen, L., and Thøgersen, M. L. (2020). Surrogate model uncertainty in wind turbine reliability assessment. *Renewable Energy*, 151:1150 – 1162.
- [72] Sriperumbudur, B., Gretton, A., Fukumizu, K., Schölkopf, B., and Lanckriet, G. (2010). Hilbert Space Embeddings and Metrics on Probability Measures. *J. Mach. Learn. Res.*, 11:1517–1561.
- [73] Stieng, L. and Muskulus, M. (2020). Reliability-based design optimization of offshore wind turbine support structures using analytical sensitivities and factorized uncertainty modeling. *Wind Energy Science*, 5:171–198.
- [74] Székely, G. J. and Rizzo, M. L. (2013). Energy statistics: A class of statistics based on distances. *Journal of Statistical Planning and Inference*, 143:1249 – 1272.
- [75] Teixeira, R., O'Connor, A., Nogal, M., Nandakumar, K., and Nichols, J. (2017). Analysis of the design of experiments of offshore wind turbine fatigue reliability design with Kriging surfaces. *Procedia Structural Integrity*, 5:951 – 958.
- [76] Van den Bos, L. (2020). *Quadrature Methods for Wind Turbine Load Calculations*. PhD thesis, Delft University of Technology.
- [77] Vanem, E., Fekhari, E., Dimitrov, N., Kelly, M., Cousin, A., and Guiton, M. (to appear in 2023). A joint probability distribution model for multivariate wind and wave conditions. In *Proceedings of the ASME 2023 42th International Conference on Ocean, Offshore and Arctic Engineering*.
- [78] Velarde, J., Kramhøft, C., and Sørensen, J. (2019). Global sensitivity analysis of offshore wind turbine foundation fatigue loads. *Renewable Energy*, 140:177 – 189.
- [79] Waarts, P. (2000). *Structural reliability using finite element methods: an appraisal of directional adaptive response surface sampling (DARS)*. PhD thesis, Technical University of Delft, The Netherlands.

- [80] Wilkie, D. and Galasso, C. (2021). Gaussian process regression for fatigue reliability analysis of offshore wind turbines. *Structural Safety*, 88:102020.
- [81] Yun, W., Lu, Z., Zhang, Y., and Jiang, X. (2018). An efficient global reliability sensitivity analysis algorithm based on classification of model output and subset simulation. *Structural Safety*, 74:49–57.
- [82] Zwick, D. and Muskulus, M. (2015). The simulation error caused by input loading variability in offshore wind turbine structural analysis. *Wind Energy*, 18:1421 – 1432.

## **Appendix A**

### **Multivariate distribution modeling**



## **Appendix B**

### **Nonparametric copula estimation**



## **Appendix C**

### **Rare event estimation algorithms**



## **Appendix D**

### **Résumé étendu de la thèse**

